

Adaptive Scan for Atomic Force Microscopy Based on Online Optimisation: Theory and Experiment

Kaixiang Wang, Michael G. Ruppert, Chris Manzie, Dragan Nešić, and Yuen K. Yong

Abstract—A major challenge in Atomic Force Microscopy (AFM) is to reduce the scan duration while retaining the image quality. Conventionally, the scan rate is restricted to a sufficiently small value in order to ensure a desirable image quality as well as a safe tip-sample contact force. This usually results in a conservative scan rate for samples that have a large variation in aspect ratio and/or for scan patterns that have a varying linear velocity. In this paper, an adaptive scan scheme is proposed to alleviate this problem. A scan line-based performance metric balancing both imaging speed and accuracy is proposed, and the scan rate is adapted such that the metric is optimised online in the presence of aspect ratio and/or linear velocity variations. The online optimisation is achieved using an extremum-seeking (ES) approach, and a semi-global practical asymptotic stability (SGPAS) result is shown for the overall system. Finally, the proposed scheme is demonstrated via both simulation and experiment.

Index Terms—Atomic force microscopy, adaptive scan, extremum-seeking control.

I. INTRODUCTION

Atomic Force Microscopy (AFM) is used to image nano-scale samples such as biological and chemical structures [1], [2]. The instrument works by scanning a cantilever over the sample surface laterally while maintaining the vertical interaction force between the cantilever tip and the sample. In order to obtain an accurate estimate of the sample topography, a vertical actuation and feedback system is typically in place to regulate the tip-sample interaction force to some set point, and the displacement of the actuator is then inverted to obtain the sample topography image [3].

There is a desire to increase the AFM imaging speed in order to achieve a higher throughput, ultimately leading to video-rate imaging. However, this is limited by the XY scanning system and vertical force regulation system [4]. The XY scanning system typically drives piezoelectric actuators to track the XY reference trajectories which form a scan pattern that suitably covers the scan area. Due to the inherent nonlinearities in piezoelectric actuators such as creep and hysteresis, feedback methods are typically implemented to ensure a good tracking performance [5]–[7]. However, the closed-loop bandwidth is limited by the lightly damped resonances

of the actuators, which in turn limits the bandwidth of the scan [8]. This is exacerbated by the use of conventional raster scan, since the triangular trajectory possesses a high waveform bandwidth [9].

To alleviate this problem, various non-raster scan patterns that are composed of low-bandwidth scan trajectories have been proposed [10]–[12]. Relevant output regulation controllers (sometimes referred to as internal model controllers or servocompensators) are designed to further increase the tracking performance [13], [14]. Additionally, combined feed-forward/feedback schemes have been proposed to overcome the limitations in feedback controller design [15], [16].

In addition to the XY scanning system, the vertical regulation system also limits the imaging speed. In order to obtain an accurate topography estimate, the regulation error needs to be small. However, the scanning motion and the varying sample topography in effect generate a disturbance to the system whose signal bandwidth increases with the scan rate. Therefore, for a given regulation system, the only way to improve the imaging accuracy is to decrease the scan rate [17].

One way to overcome this limitation is to increase the Z feedback loop bandwidth through novel actuator designs and/or high-bandwidth robust controller designs [18]–[21]. Alternatively, the underlying connection between XY and Z systems can be utilised. The scan is usually conducted in a line-by-line manner with two consecutive scan lines very close to each other. This implies that the sample topography signal along two consecutive lines would be similar. Several researchers have attempted to utilise this characteristic and devised iterative, repetitive or feedforward controllers to improve the vertical regulation response [22]–[24].

All aforementioned methods assume a fixed scan rate. This may lead to a conservative imaging speed for samples that have a large variation in aspect ratio and/or scan patterns that have a varying linear velocity. The scan rate needs to be sufficiently small to ensure a small regulation error and safe contact force even in the worst case [17]. Therefore, it is desirable to adapt the scan rate to these variations in order to achieve a faster imaging speed while retaining a desirable image quality.

A few rule-based adaptive scan methods have been proposed in [25]–[27]. However, these methods react to the instantaneous regulation error and are not concerned with the optimality of scan. In [28], we have proposed a novel adaptive scan scheme based on the online optimisation of a performance metric. Representing the trade-off between imaging speed and accuracy, the metric can be a user-specified function of the scan rate and regulation error over each line to suit particular

Kaixiang Wang is with the Department of Mechanical Engineering, The University of Melbourne, Parkville, VIC 3010, Australia. (e-mail: kaixiangw@student.unimelb.edu.au).

Michael G. Ruppert and Yuen K. Yong are with the School of Electrical Engineering and Computing, The University of Newcastle, Callaghan, NSW 2308, Australia (e-mail: michael.ruppert@newcastle.edu.au; yuenkuan.yong@newcastle.edu.au).

Chris Manzie and Dragan Nešić are with the Department of Electrical and Electronic Engineering, The University of Melbourne, Parkville, VIC 3010, Australia. (e-mail: manziec@unimelb.edu.au; dnesic@unimelb.edu.au).

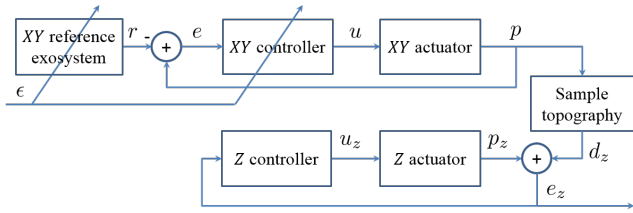


Fig. 1. AFM system block diagram.

applications. As one potential choice, the performance metric can penalise the deviation of the maximum regulation error over a line from some set point. In this way, it is expected that a better image can be obtained under a certain duration, thereby improving the imaging speed-accuracy trade-off. Since the sample topography is unknown, the optimal scan rate that optimises the metric is in general unknown. Therefore, in [28], we have implemented the extremum-seeking (ES) framework in [29] to search for the unknown optimal scan rate. Due to sample topography variations, the optimal scan rate is time-varying. However, since two consecutive scan lines are close to each other, the regulation error along the two lines are similar. Therefore, it is expected that the optimal scan rate is slowly varying across scan lines. In [28], we have shown via simulation that the algorithm may track the optimal scan rate approximately and retain a semi-global practical asymptotic stability (SGPAS).

This paper extends our preliminary work presented in [28] both theoretically and experimentally. In this paper, a rigorous theoretical proof is given for the SGPAS result, which in itself is a nontrivial extension of that in [29] due to the consideration of a time-varying cost function. Secondly, a systematic comparison between the proposed adaptation law and the existing adaptation law in [27] is performed, and indicates superior performance of the proposed method. Thirdly, this paper discusses a practical scenario where the adaptive scan scheme can be used to improve the imaging performance. Finally, the adaptive scan scheme is implemented on a commercial AFM platform, demonstrating the efficacy of the proposed approach.

The rest of this paper is organized as follows. In Section II, the AFM system is introduced and the performance function is defined. In Section III, the adaptation law is described based on the design of an ES controller that optimises the performance function, and the SGPAS result is shown. The simulation and experiment results are presented in Section IV and V, respectively. Finally, conclusions are drawn in Section VI.

II. PROBLEM FORMULATION

In this section, the AFM system is introduced and the performance function is defined. A few mathematical assumptions are posed in order to facilitate forthcoming theoretical performance analysis.

A. System Model

Consider a typical AFM system structure illustrated in Fig. 1. $r \in \mathbb{R}^2$ denotes the XY reference trajectories, $u \in \mathbb{R}^2$ the

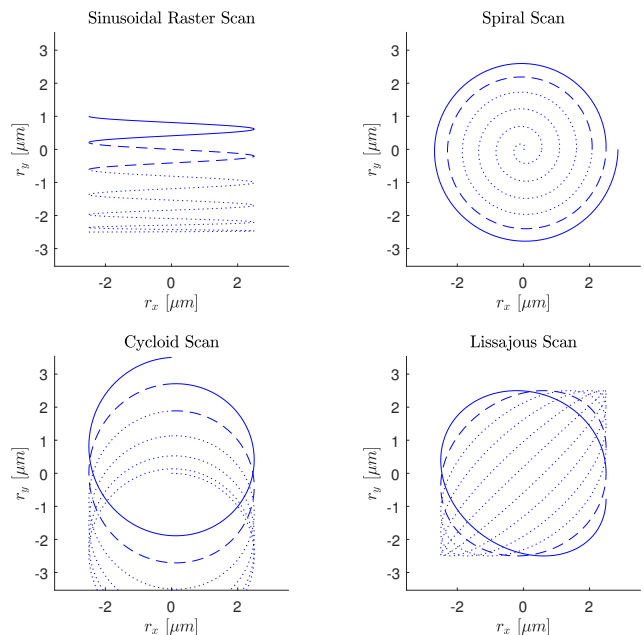


Fig. 2. Definition of scan lines. The solid and dashed lines represent a set of current and previous scan lines, respectively.

XY control inputs, $p \in \mathbb{R}^2$ the XY actuator displacements and $e \in \mathbb{R}^2$ the XY tracking error. The sample topography relates the XY actuator displacements to the sample topography signal $d_z \in \mathbb{R}$, which acts as an output disturbance to the vertical feedback system. $u_z \in \mathbb{R}$, $p_z \in \mathbb{R}$ and $e_z \in \mathbb{R}$ represent the control input, actuator displacement, and regulation error along the Z axis, respectively. The XY and Z controllers are designed to minimise e and e_z , respectively.

A range of scan patterns are available in the literature: conventional raster or sinusoidal raster scan, cycloid scan [10], spiral scan [11], and Lissajous scan [12]. All these scan methods are conducted in a line-by-line manner and each line is referred to as a *scan line* (see Fig. 2). The nominal duration for completing a scan line is referred to as the *nominal line period* and is denoted by T_l . In practice, it is usually possible to modify the *number of scan lines*, N , which would affect the *nominal scan duration*, T_0 . Moreover, in order to trade off between speed and accuracy, it is also possible to vary the duration for completing a scan line, or the *line period*, by modifying the *scan rate multiplier*, ϵ . Both N and ϵ affect the scan duration.

Assumption 1: The XY references trajectories can be generated by a linear neutrally stable exosystem model:

$$\begin{aligned} \dot{\xi}_r &= \epsilon A_r(N) \xi_r, \\ r &= C_r \xi_r, \end{aligned} \quad (1)$$

where $\xi_r \in D_r \subset \mathbb{R}^{n_r}$ denotes the exosystem state, and $A_r(N)$ and C_r are matrices that determine the shape of the scan path. Notice that the dependence of A_r on N reflects the fact that the shape of the scan path depends on the number of scan lines.

Remark 1: All aforementioned scan patterns have reference trajectories that can be cast into or approximated by the above

form (1) with appropriate initial conditions [17]. It should be noted that although the triangular trajectory may be present in some of the scan patterns, they can be approximated by a finite sum of sinusoids whose frequency is the odd harmonics of the fundamental frequency [30], which is then compatible with (1). This approximation can simplify subsequent analysis, but is not required for the implementation of the proposed scheme in practice, as will be shown in the simulation result section.

Since ϵ could be time-varying, to facilitate the forthcoming analysis, an auxiliary timescale τ is defined by

$$\dot{\tau} = \epsilon(t) \quad (2)$$

with $\tau(0) = 0$. It can be seen that this definition reduces to $\tau = \epsilon t$ for a constant ϵ , and that $\tau(t)$ is invertible as long as $\epsilon(t)$ is positive for all $t \geq 0$.

Remark 2: τ can be seen as the distance, rather than the duration, that the scan has progressed. This should be clear by rewriting (1) in the τ -timescale,

$$\frac{d\xi_r}{d\tau} = A_r(N) \xi_r, \quad (3)$$

and noticing its solution does not depend on ϵ .

Since the forthcoming analysis will mainly be done in the τ -timescale, the following abuse of notation is used to simplify the presentation. For an arbitrary signal $y(t)$ and its trajectory in the τ -timescale defined by $y_\tau(\tau) \triangleq y(t(\tau))$, the subscript will be dropped when there is no confusion, i.e. $y_\tau(\tau)$ is simply written as $y(\tau)$.

Now, two examples of the reference trajectories are provided below given the scan size¹ L , the nominal line period T_l and the number of scan lines N . Also define $A_l = \frac{L}{2}$, $\omega_l = \frac{2\pi}{T_l}$, $\omega_{fr} = \frac{2\pi}{(2N-1)T_l}$ and $\omega_{fs} = \frac{2\pi}{4NT_l}$.

Example 1: The sinusoidal raster scan reference trajectories can be generated by

$$\begin{aligned} r_x(\tau) &= A_l \sin\left(\omega_l \tau - \frac{\pi}{2}\right), \\ r_y(\tau) &= A_l \sin\left(\omega_{fr} \tau - \frac{\pi}{2}\right), \end{aligned}$$

which can be realised by a model in the form of (3) with

$$\begin{aligned} A_r &= \begin{bmatrix} 0 & \omega_l & 0 & 0 \\ -\omega_l & 0 & 0 & 0 \\ 0 & 0 & 0 & \omega_{fr} \\ 0 & 0 & -\omega_{fr} & 0 \end{bmatrix}, \quad \xi_r(0) = \begin{bmatrix} -A_l \\ 0 \\ -A_l \\ 0 \end{bmatrix}, \\ C_r &= \begin{bmatrix} 1 & 0 & 0 & 0 \\ 0 & 0 & 1 & 0 \end{bmatrix}. \end{aligned}$$

Example 2: Likewise, the spiral scan reference trajectories are²

$$\begin{aligned} r_x(\tau) &= A_l \sin(\omega_{fs} \tau) \cos(\omega_l \tau), \\ r_y(\tau) &= A_l \sin(\omega_{fs} \tau) \sin(\omega_l \tau). \end{aligned}$$

¹The side length of a square scan area.

²The proposed spiral scan trajectories are different from those in [11], [14] in the sense that they are sinusoidally modulated rather than triangularly modulated.

Using the trigonometric identity, they are equivalent to

$$\begin{aligned} r_x(\tau) &= \frac{1}{2} A_l (\sin((\omega_l + \omega_{fs}) \tau) - \sin((\omega_l - \omega_{fs}) \tau)), \\ r_y(\tau) &= \frac{1}{2} A_l (\cos((\omega_l - \omega_{fs}) \tau) - \cos((\omega_l + \omega_{fs}) \tau)), \end{aligned}$$

which can be similarly generated using (3).

The following assumption is placed on the sample topography to facilitate forthcoming analysis.

Assumption 2: The sample topography is represented by a static map, $f_s: \mathbb{R}^2 \rightarrow \mathbb{R}$, which is unknown but is sufficiently many times differentiable.

Remark 3: In practice, the sample can have vertical edges or even overhanging features. However, the shape and size of the cantilever tip as well as the tip cone angle inevitably produce some apparent slope. Therefore, despite the apparent limiting nature of this mathematical assumption, from a practical viewpoint it is not a significant impediment.

Consider the XY actuator

$$\begin{aligned} \dot{\xi}_o &= A_o \xi_o + B_o u \\ p &= C_o \xi_o, \\ e &= p - r \end{aligned} \quad (4)$$

the XY controller

$$\begin{aligned} \dot{\xi}_c &= A_c(\epsilon, N) \xi_c + B_c(\epsilon, N) e, \\ u &= C_c(\epsilon, N) \xi_c \end{aligned} \quad (5)$$

the Z actuator

$$\begin{aligned} \dot{\xi}_{zo} &= A_{zo} \xi_{zo} + B_{zo} u_z \\ p_z &= C_{zo} \xi_{zo}, \\ e_z &= p_z + f_s(p) \end{aligned} \quad (6)$$

and the Z controller

$$\begin{aligned} \dot{\xi}_{zc} &= A_{zc} \xi_{zc} + B_{zc} e_z, \\ u_z &= C_{zc} \xi_{zc} \end{aligned} \quad (7)$$

where $\xi_o \in \mathbb{R}^{n_o}$ and $\xi_c \in \mathbb{R}^{n_c}$ represent the XY actuator and controller state variables, respectively, and $\xi_{zo} \in \mathbb{R}^{n_{zo}}$, $\xi_{zc} \in \mathbb{R}^{n_{zc}}$ the Z counterparts.

Remark 4: It is common to model the actuators with linear models preceded by hysteresis nonlinearity [31]–[33]. Although the form of (4) and (6) here neglects the hysteresis effect, it is assumed that the hysteresis can be cancelled by means of hysteresis inversion [31] or charge drives [34].

Remark 5: The XY controller (5) and Z controller (7) are stated in a general form to cover a wide range of existing control algorithms on these axes with the adaptive scan augmentation. Their designs are not the intended contribution of this paper. The dependence of (5) on ϵ and N is in order to permit asymptotic tracking. A similar construct appears in [35], where the argument of the system matrices is the online estimate of a presumably unknown frequency for the exogenous reference and disturbance.

Example 3: In [35], the authors propose a controller for single-input-single-output linear time-invariant systems to

asymptotically track reference trajectories or reject disturbances of certain frequency ω . The controller is parameterised by the frequency and has the transfer function of

$$G_c(s) = D(s)C(s),$$

where $D(s)$ a stabilising controller for the closed-loop system in the absence of $C(s)$, and

$$C(s) = \frac{s^2 + 2\zeta\omega s + \omega^2}{s^2 + \omega^2} \quad (8)$$

is a notch-like internal model controller that enables asymptotic regulation. It is shown in [35] that the closed-loop with the inclusion of $C(s)$ remains stable for sufficiently small ζ and ω . It can be checked that $G_c(s)$ can be realised in the form of (5) when ω is a function of ϵ and/or N .

The following assumption is placed on the AFM system dynamics. For the ease of notation, denote $x \triangleq (\xi_o, \xi_c, \xi_{zo}, \xi_{zc})$ and rewrite (4)–(7) in the τ -timescale as follows:

$$\frac{dx}{d\tau} = f(x, \xi_r, \epsilon, N), \quad (9)$$

$$e = h(x, \xi_r), \quad (10)$$

$$e_z = h_z(x), \quad (11)$$

where the specific forms of f , h and h_z are omitted for space reasons.

Assumption 3: There exist $\bar{\epsilon}, \underline{N} > 0$ such that for each $0 < \epsilon \leq \bar{\epsilon}$ and $N \geq \underline{N}$ and each $\xi_r(0) \in D_r$ of (3), the AFM system dynamics (9) has a uniformly globally asymptotically stable (UGAS) steady-state solution $\bar{x}(\tau)^3$ which satisfies that

- 1) there exists a sufficiently smooth map M such that

$$\bar{x}(\tau) = M(\xi_r(\tau), \epsilon, N)$$

holds for $\tau \in \mathbb{R}$;

- 2) the steady-state XY tracking error denoted by $\bar{e}(\tau) \triangleq h(\bar{x}(\tau), \xi_r(\tau))$ satisfies

$$\bar{e}(\tau) = 0$$

for $\tau \in \mathbb{R}$; and

- 3) there exists some constant $k_e > 0$ such that the steady-state Z regulation error $\bar{e}_z(\tau) \triangleq h_z(\bar{x}(\tau))$ satisfies

$$|\bar{e}_z(\tau + T_l) - \bar{e}_z(\tau)| \leq \frac{k_e}{N}$$

for $\tau \in \mathbb{R}$.

Moreover, there exist functions $\alpha_{x1}, \alpha_{x2} \in \mathcal{K}_\infty, \alpha_f \in \mathcal{K}$ and a smooth Lyapunov function $V_x(\tilde{x}, \epsilon, N)$ such that for each $0 < \epsilon \leq \bar{\epsilon}, N \geq \underline{N}$ and $\xi_r(0) \in D_r$,

$$\begin{aligned} \alpha_{x1}(|\tilde{x}|) &\leq V_x(\tilde{x}, \epsilon, N) \leq \alpha_{x2}(|\tilde{x}|) \\ \frac{\partial V_x}{\partial \tilde{x}} \tilde{f}(\tilde{x}, \xi_r(\tau), \epsilon, N) &\leq -\alpha_f(|\tilde{x}|) \end{aligned}$$

holds for all $\tau \geq 0$, where $\tilde{x} \triangleq x - M(\xi_r(\tau), \epsilon, N)$ and $\tilde{f}(\tilde{x}, \xi_r(\tau), \epsilon, N) \triangleq f(\tilde{x} + M(\xi_r(\tau), \epsilon, N), \xi_r(\tau), \epsilon, N) - f(M(\xi_r(\tau), \epsilon, N), \xi_r(\tau), \epsilon, N)$.

³Notice the dependence of $\bar{x}(\tau)$, $\bar{e}(\tau)$ and $\bar{e}_z(\tau)$ on ϵ, N and $\xi_r(0)$ is dropped to ease the notation.

Remark 6: Due to linearity, the XY subsystem (4)–(5) and the Z subsystem (6)–(7) can be stabilised under mild assumptions on the actuator dynamics. For the same reason, it can be seen that the stabilised AFM system (9) is *uniformly convergent with the uniformly bounded steady-state property* [36] with respect to bounded continuous input signals, and the existence of the map M follows from [36, Theorem 2].

Remark 7: Zero steady-state XY tracking error can be achieved by output regulation controllers based on some practical assumptions on the reference trajectory model (1) and the XY actuator dynamics (4). See [13], [14], [35] for nanopositioning applications and [37] for linear systems in general. This may not be achievable in practice, but this does not obstruct the implementation of the proposed scheme in general, as will be shown in the simulation result section.

Remark 8: For the aforementioned scan patterns, two consecutive scan lines are typically very close in order to achieve a high image resolution. This implies that the topography signal, and therefore the Z regulation error, would be close to periodic with the period T_l in the τ -timescale. Moreover, as the number of scan lines increases, the differences between two consecutive lines and between the corresponding regulation errors would decrease. This observation is the key to the proposed adaptive scan.

Remark 9: The requirement on existence of α_{x1}, α_{x2} and α_f being independent of N may be difficult to satisfy for arbitrarily large N . In practice, however, N is upper bounded by the finite resolution of the XY subsystem and hence α_{x1}, α_{x2} and α_f be established for the largest possible N .

B. Definition of Performance Function

In order to generalise the intuitive performance metric mentioned in Section I, the performance function is assumed to have the form of

$$q(\tau) = Q(e_z[\tau], \epsilon[\tau]) \quad (12)$$

$$\triangleq g_e(L_e(e_z[\tau])) + g_s(L_s(\epsilon[\tau])),$$

where g_e and g_s are arbitrary sufficiently smooth functions and L_e and L_s are defined by

$$L_e(e_z[\tau]) \triangleq \begin{cases} \left(\frac{1}{T_l} \int_{\tau-T_l}^{\tau} |e_z(\sigma)|^p d\sigma \right)^{\frac{1}{p}} & p \in [1, \infty) \\ \max_{\sigma \in [\tau-T_l, \tau]} |e_z(\sigma)| & p = \infty \end{cases}, \quad (13)$$

$$L_s(\epsilon[\tau]) \triangleq \epsilon(\tau - \tau_\phi), \quad (14)$$

respectively. Specifically, $L_e(e_z[\tau])$ is the L_p -norm characterisation of the line regulation error, and $L_s(\epsilon[\tau])$ is the delayed scan rate, where p is a design parameter and $\tau_\phi \in [0, T_l]$ is a small constant to match the effective time delays between these two channels. The functions g_e and g_s can be chosen to suit application-specific imaging goals and requirements, e.g. minimising the deviation from some target local imaging accuracy. Mathematically, the arguments of Q are histories of regulation error and scan rate: $e_z[\tau] \triangleq \{e_z(\tau + \sigma) : \sigma \in [-\tau_d, 0]\}$ and $\epsilon[\tau] \triangleq \{\epsilon(\tau + \sigma) : \sigma \in [-\tau_d, 0]\}$ with $\tau_d = T_l + \frac{2\pi}{\omega}$ being the length of the histories, where ω is defined later.

In steady state, the relation between fixed values of ϵ , N and q can be defined by the following time-varying map for all $\tau \in \mathbb{R}$:

$$\bar{J}(\epsilon, N, \tau) \triangleq g_e \left(\left(\frac{1}{T_l} \int_{\tau-T_l}^{\tau} |h_z(M(\xi_r(\sigma), \epsilon, N))|^p d\sigma \right)^{\frac{1}{p}} \right) + g_s(\epsilon).$$

Assumption 4: The following holds:

- $\bar{J}(\epsilon, N, \tau)$, $\frac{\partial \bar{J}}{\partial \epsilon}(\epsilon, N, \tau)$ and $\frac{\partial^2 \bar{J}}{\partial \epsilon^2}(\epsilon, N, \tau)$ are bounded for all $0 < \epsilon \leq \bar{\epsilon}$ and $N \geq \underline{N}$ uniformly in $\tau \in \mathbb{R}$.
- $\bar{J}(\epsilon, N, \tau)$ has a maximum at the solution $\epsilon^*(N, \tau)$ for each $N \geq \underline{N}$ and $\tau \in \mathbb{R}$.
- There exists $\alpha_J \in \mathcal{K}$ such that

$$\frac{\partial \bar{J}}{\partial \epsilon}(\epsilon, N, \tau) (\epsilon - \epsilon^*(N, \tau)) \leq -\alpha_J (|\epsilon - \epsilon^*(N, \tau)|)$$

holds for all $0 < \epsilon \leq \bar{\epsilon}$, $N \geq \underline{N}$ and $\tau \in \mathbb{R}$.

- There exist $\underline{\epsilon}^*, \bar{\epsilon}^* \in (0, \bar{\epsilon}]$ such that $\underline{\epsilon}^* \leq \epsilon^*(N, \tau) \leq \bar{\epsilon}^*$ holds for all $N > \underline{N}$ and $\tau \in \mathbb{R}$.

Remark 10: The satisfaction of Assumption 4 depends on the sample topography, the AFM system dynamics and the design of g_e and g_s . In general, it may be difficult to analytically verify Assumption 4. However, an example is given in Section IV using a carefully constructed sample.

Assumption 5: The functions $\bar{J}(\epsilon, N, \tau)$ and $\epsilon^*(N, \tau)$ are continuously differentiable in τ . Moreover, there exist $k_J, k_\epsilon > 0$ such that

$$\begin{aligned} \left| \frac{\partial \bar{J}}{\partial \tau} \right| &\leq \frac{k_J}{N}, \\ \left| \frac{\partial \epsilon^*}{\partial \tau} \right| &\leq \frac{k_\epsilon}{N}, \end{aligned}$$

for all $0 < \epsilon \leq \bar{\epsilon}$ and $N \geq \underline{N}$ uniformly in $\tau \in \mathbb{R}$.

Remark 11: Assumption 5 states that the steady-state cost map and optimal scan rate trajectory become less time-dependent as the number of scan lines N increases. Indeed, as N approaches infinity, the scan is conducted over the same scan line, yielding a constant steady-state cost map and optimal scan rate solution.

III. ADAPTATION LAW DESIGN

The performance function defines a unique optimal scan rate trajectory. Since the sample topography is unknown, the optimal trajectory is also unknown. Therefore, an adaptation law is devised to search for the optimal scan rate trajectory based on the extremum-seeking approach. Theoretical performance guarantees are then provided by conducting stability analysis on the overall system.

A. Extremum-Seeking Controller

The closed-loop system is illustrated in Fig. 3. As in [29], a dither is added to the estimate of ϵ^* , $\hat{\epsilon}$, yielding $\epsilon = \hat{\epsilon} + a \sin(\omega\tau)$, where a is the dither amplitude and ω is the dither frequency. Notice the dither is based in the τ -timescale and τ can be obtained by integrating ϵ with respect to t (see (2)).

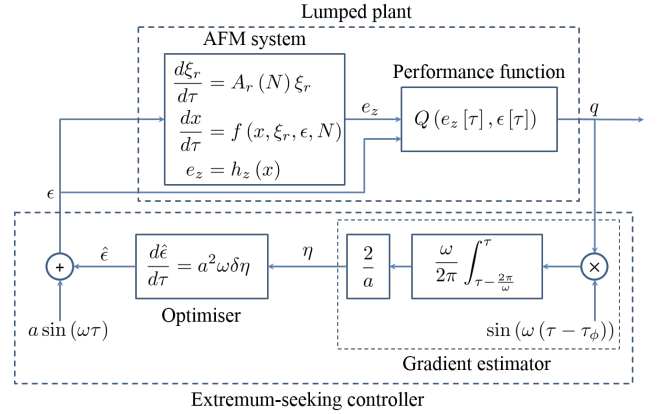


Fig. 3. Overall system block diagram. Notice that the plant is represented in the τ -timescale, and the performance function, dither, gradient estimator and optimiser are all based in the τ -timescale.

Then, the resulting performance output from the lumped plant is passed through a mean-over-perturbation-period (MOPP) filter that is used for gradient estimation:

$$\eta(\tau) = \frac{\omega}{a\pi} \int_{\tau-\frac{2\pi}{\omega}}^{\tau} q(\sigma) \sin(\omega(\sigma - \tau_\phi)) d\sigma, \quad (15)$$

where η is the estimated gradient of \bar{J} and τ_ϕ is defined earlier. Unlike commonly used finite-order low/high-pass filters, the MOPP completely filters out the higher-order harmonics of ω , thus improving the accuracy of gradient estimation and increasing the convergence speed [29].

Finally, the optimiser has the form of

$$\frac{d\hat{\epsilon}}{d\tau} = a^2 \omega \delta \eta, \quad (16)$$

where $\delta > 0$ is a constant parameter.

Remark 12: Increasing a , ω and δ can increase the adaptation speed, however, large a and ω result in a larger and faster steady-state performance metric fluctuation, respectively. Moreover, to ensure stability, ω needs to be sufficiently smaller than ω_l to ensure timescale separation between lumped plant dynamics and gradient estimation, and similarly, δ needs to be sufficiently small to ensure timescale separation between gradient estimation and scan rate optimisation. A qualitative guideline on parameter tunings that is sufficient for the overall system stability is given in Theorem 1.

Remark 13: The implementation of the adaptive scan scheme requires the evaluations of (2) and (12)–(16), which only involve two numerical integrations, one moving L_p -norm evaluation and one moving average evaluation. Therefore, the implementation of the adaptive scan scheme does not pose significant computational requirements.

B. Stability Analysis

Next, the SGPAS result is to be established in the τ timescale. To begin, define $\tilde{x} = x - M(\xi_r, \epsilon, N)$ and $\tilde{\epsilon} = \hat{\epsilon} - \epsilon^*(N, \tau)$, and the overall system (3), (9), (11)–(16) can

be described as follows:

$$\frac{d\xi_r}{d\tau} = A_r(N) \xi_r, \quad (17)$$

$$\frac{d\tilde{x}}{d\tau} = \tilde{f}(\tilde{x}, \xi_r, \epsilon, N) - \frac{\partial M}{\partial \epsilon} \left(\frac{d\hat{\epsilon}}{d\tau} + a\omega \cos(\omega\tau) \right), \quad (18)$$

$$\begin{aligned} \frac{d\tilde{\epsilon}}{d\tau} &= \frac{a\omega^2\delta}{\pi} \int_{\tau-\frac{2\pi}{\omega}}^{\tau} J(\tilde{x}[\sigma], \xi_r[\sigma], \epsilon[\sigma], N) s(\sigma) d\sigma \\ &\quad - \frac{\partial \epsilon^*}{\partial \tau}(N, \tau), \end{aligned} \quad (19)$$

where $\tilde{f}(\tilde{x}, \xi_r, \epsilon, N)$ is defined in Assumption 3, $J(\tilde{x}[\tau], \xi_r[\tau], \epsilon[\tau], N) \triangleq Q(h_z(\tilde{x}[\tau] + M(\xi_r[\tau], \epsilon[\tau], N)), \epsilon[\tau])$ with $\tilde{x}[\tau]$ and $\xi_r[\tau]$ defined in the same way as $\epsilon[\tau]$, and $s(\tau) \triangleq \sin(\omega(\tau - \tau_\phi))$.

Theorem 1: Suppose Assumptions 1–5 hold, then for each $\rho_x^0, \rho_\epsilon^0 > 0$, each $\nu_\epsilon^+ \in (0, \frac{\bar{\epsilon}}{2})$ and each $\nu_x, \nu_\epsilon > 0$, there exist $\rho_x, \rho_\epsilon > 0$ and $a^* > 0$ such that for each $a \in (0, a^*)$ there exists $\omega^* > 0$ such that for each $\omega \in (0, \omega^*)$ there exists $\delta^* > 0$ such that for each $\delta \in (0, \delta^*)$ such that there exists $N^* > 0$ such that for each $N \in (N^*, \infty)$ and each initial condition $(\tilde{x}[0], \tilde{\epsilon}[0])$ such that $\begin{bmatrix} |\tilde{x}[0]| \\ |\tilde{\epsilon}[0]| \end{bmatrix} \leq \begin{bmatrix} \rho_x^0 \\ \rho_\epsilon^0 \end{bmatrix}$ and $\nu_\epsilon^+ \leq \hat{\epsilon}(0) \leq \bar{\epsilon} - \nu_\epsilon^+$, the solution of (17)–(19) satisfies

$$\sup_{\tau \geq 0} \begin{bmatrix} |\tilde{x}(\tau)| \\ |\tilde{\epsilon}(\tau)| \end{bmatrix} \leq \begin{bmatrix} \rho_x \\ \rho_\epsilon \end{bmatrix} \quad \text{and} \quad \limsup_{\tau \rightarrow \infty} \begin{bmatrix} |\tilde{x}(\tau)| \\ |\tilde{\epsilon}(\tau)| \end{bmatrix} \leq \begin{bmatrix} \nu_x \\ \nu_\epsilon \end{bmatrix}$$

and $0 < \epsilon(\tau) < \bar{\epsilon}$ for all $\tau \geq 0$.

Proof: See Appendix. ■

Corollary 1: Under the conditions of Theorem 1, the solution of (17)–(19) satisfies

$$\sup_{t \geq 0} \begin{bmatrix} |\tilde{x}(t)| \\ |\tilde{\epsilon}(t)| \end{bmatrix} \leq \begin{bmatrix} \rho_x \\ \rho_\epsilon \end{bmatrix} \quad \text{and} \quad \limsup_{t \rightarrow \infty} \begin{bmatrix} |\tilde{x}(t)| \\ |\tilde{\epsilon}(t)| \end{bmatrix} \leq \begin{bmatrix} \nu_x \\ \nu_\epsilon \end{bmatrix}.$$

Remark 14: Theorem 1 together with Corollary 1 states the SGPAS of the overall system and signifies that the XY tracking errors converge to a neighbourhood of zero and the estimate of optimal scan rate converges to a neighbourhood of the true value provided parameters a, ω, δ and N are properly tuned. Specifically, for an arbitrarily small given neighbourhood, a sufficiently small a is firstly selected, based on which then a sufficiently small ω is selected, based on which a sufficiently small δ is selected, and finally based on which a sufficiently large N is selected. These selections of parameters can then ensure the convergence to such a small neighbourhood.

Remark 15: As noted in Remark 9, there is a finite upper bound to the number of scan lines, N , in any practical system. This limits the explicit implementation of the theorem.

However, in practice this is not a significant imposition for real systems as will be seen in the following result sections.

Remark 16: Although the initial condition $\hat{\epsilon}(0)$ cannot be selected arbitrarily on \mathbb{R} due to realistic constraints on the scan rate, the set of permissible initial conditions can become arbitrarily close to the set of permissible scan rate of the original system as specified in Assumption 3, hence the term ‘semi-global’.

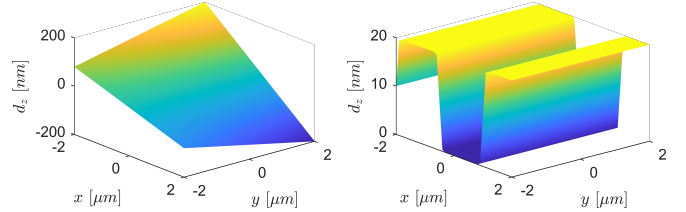


Fig. 4. Sample topography. Scenario One: a tilted and bent plane (left). Scenario Two: periodic rectangular features (right).

IV. SIMULATION RESULTS

Simulation studies are conducted based on two scenarios to verify the theoretical results as well as to provide motivating scenarios under which the adaptive scan is desirable. Specifically, Scenario One provides a thorough exposition of the theoretical results by studying a constructed sample, and Scenario Two suggests a solution to the known issue of varying linear velocity and resulting imaging accuracy during a spiral scan. For both scenarios, the linear models (20)–(22) are used for the X, Y and Z actuators, respectively.

A. Scenario One: Constructed Sample and Sinusoidal Raster Scan

In this scenario, the sample topography map (Fig. 4, left) represents a tilted and bent plane whose magnitude of the gradient along X increases along Y. The map has the expression of $f_s(x, y) = -(15y + 70)x$. The sinusoidal raster scan in Example 1 is conducted with a scan size of $L = 4 \mu\text{m}$ and a nominal line period of $T_l = 0.01$ s. This suggests a nominal scan duration of $T_0 = 0.995$ s if $N = 100$. It can be shown that Assumptions 1 and 2 are satisfied.

The XY controller design follows Example 3. The stabilising controllers for X and Y axes are both $D(s) = \frac{667}{s}$. The X internal model controller is designed with $\zeta_{xc} = 1$ and $\omega_{xc} = \epsilon\omega_l$. A slight modification is made for the Y internal model controller design to enhance convergence, resulting the controller $C_y(s) = \frac{(s+500(\epsilon\omega_{fr}))^2}{s^2 + (\epsilon\omega_{fr})^2}$. For the Z axis, an integral controller is used with a gain of 7.14×10^3 . It can

$$G_{x_o}(s) = \frac{245s^2 - 2.73 \times 10^6 s + 2.9 \times 10^{10}}{s^3 + 1796s^2 + 3.39 \times 10^7 s + 5.64 \times 10^{10}}, \quad (20)$$

$$G_{y_o}(s) = \frac{241s^4 - 3.18 \times 10^6 s^3 + 4.26 \times 10^{10} s^2 - 9.41 \times 10^{13} s + 1.13 \times 10^{18}}{s^5 + 2328s^4 + 6.79 \times 10^7 s^3 + 1.45 \times 10^{11} s^2 + 1.14 \times 10^{15} s + 2.21 \times 10^{18}}, \quad (21)$$

$$G_{z_o}(s) = \frac{64.6s^4 - 2.77 \times 10^5 s^3 + 5.27 \times 10^{11} s^2 - 3.41 \times 10^{16} s + 1.5 \times 10^{21}}{s^5 + 4.52 \times 10^4 s^4 + 3.64 \times 10^9 s^3 + 1.14 \times 10^{11} s^2 + 3 \times 10^{18} s + 3.16 \times 10^{22}}. \quad (22)$$

be checked that the controllers can be realised in the form of (5) and (7) and Assumption 3 holds for any compact subset of $N \in [\underline{N}, \infty)$.

The following performance function is used with $p = \infty$ chosen in (13):

$$Q(e_z[\tau], \epsilon) = - \left(\max_{\sigma \in [\tau - T_l, \tau]} |e_z(\sigma)| - e_z^* \right)^2$$

with $e_z^* = 4$ nm. This represents the objective of keeping the maximum regulation error for each line at 4 nm. Notice that since the movement along Y is much slower than that along X, the steady-state topography signal could be locally well approximated by a sinusoidal signal whose frequency is the actual scan rate $\omega_l \epsilon$ and whose amplitude depends on the local gradient of the sample along X, i.e.

$$\begin{aligned} A(N, \tau) &= A_l \left| \frac{\partial f_s}{\partial x} \Big|_{y=A_l \sin(\omega_{fr}\tau - \frac{\pi}{2})} \right| \\ &= \left(15A_l \sin\left(\omega_{fr}\tau - \frac{\pi}{2}\right) + 70 \right) A_l. \end{aligned}$$

Moreover, since the Z closed-loop dynamics are linear, denote the sensitivity function by $S_z(s)$, then the maximum line regulation error can be approximated by $A(N, \tau) S_z(\omega_l \epsilon)$. Finally, since $S_z(s)$ is almost linear in the passband, it may be approximated by a proportional function with an identified gain of $k_{S_z} = 2.95 \times 10^{-3}$. Therefore, the approximate steady-state cost map is

$$\hat{J}(\epsilon, N, \tau) = - (A(N, \tau) k_{S_z} \omega_l \epsilon - e_z^*)^2$$

and the approximate optimal scan rate trajectory is

$$\hat{\epsilon}^*(N, \tau) = \frac{e_z^*}{A(N, \tau) k_{S_z} \omega_l}.$$

It can be verified that Assumptions 4 and 5 are satisfied.

With Assumptions 1–5 now satisfied, it is expected that the SGPAS result from Theorem 1 holds for the closed-loop system. This is confirmed by the simulation results shown in Figs. 5 and 6 with the ES parameters $\tau_\phi = 6 \times 10^{-3}$, $a = 0.001$, $\omega = 210$ and $\delta = 2$. In Fig. 5, N is set to 100 and three sets of scans are conducted with different initial conditions $\hat{\epsilon}(0)$. It can be seen that all three trajectories of $\hat{\epsilon}(\tau)$ converge to the neighbourhood of the approximate optimal solution $\hat{\epsilon}^*(N, \tau)$. Note that in order to improve the transient behaviour, the optimiser is not turned on until $\tau = T_l + \frac{2\pi}{\omega}$. It may also be worth noting that a uniform convergence speed is attained in the τ -timescale rather than in the t -timescale.

Fig. 6 shows the adaptation error trajectory for two scans (forward and backward along Y) under different N values. It can be seen that the adaptation error reduces as N increases. Note that the X axis is normalised and represents the number of completed scans.

Finally, the performance of the adaptive scan method when $N = 100$ is compared with that of the conventional fixed-rate scan method. This is done by setting the scan rate of the fixed-rate method such that it would complete the scan under the same duration. The XY reference trajectories, XY and Z controllers remain unchanged for the fixed-rate case. The result is shown in Fig. 7. It can be seen that, despite

sample topography variations, the proposed method adjusts the scan rate to track the desired imaging accuracy, i.e. the maximum regulation error over scan lines, q_e , is maintained at about the set point $e_z^* = 4$ nm. The small oscillations of q_e and ϵ are due to the action of dithering. On the other hand, the fixed-rate method yields a considerable contrast in imaging accuracy in different regions of the sample.

B. Comparison with Existing Adaptive Scan under Conventional Raster Scan

In this subsection, the proposed adaptive scan scheme is compared with the existing adaptive scan method in [27] using the same sample. Since the latter only considers conventional raster scan pattern, the following triangular XY reference trajectories are used:

$$\begin{aligned} r_x(\tau) &= A_l \text{tri}\left(\omega_l \tau - \frac{\pi}{2}\right), \\ r_y(\tau) &= A_l \text{tri}\left(\omega_{fr} \tau - \frac{\pi}{2}\right), \end{aligned}$$

where

$$\text{tri}(\tau) \triangleq \begin{cases} \frac{2}{\pi} \tau & \tau - 2k\pi \in [0, \frac{\pi}{2}) \\ 2 - \frac{2}{\pi} \tau & \tau - 2k\pi \in [\frac{\pi}{2}, \frac{3\pi}{2}) \\ -4 + \frac{2}{\pi} \tau & \tau - 2k\pi \in [\frac{3\pi}{2}, 2\pi) \end{cases}, \quad k \in \mathbb{Z}.$$

For the proposed adaptive scan, the XY and Z controllers, performance function, and ES parameters remain unchanged. Since the XY reference trajectories are non-smooth, asymptotic tracking is not possible, and Assumptions 1 and 3 no longer hold. However, as shown in the left column of Fig. 8, the adaptive scan still manages to maintain q_e at about the set point e_z^* by adapting the scan rate.

The adaptive scan proposed in [27] is then implemented for comparison. The same XY and Z controllers are used. It should be noted that [27] combines a few field-specific insights into its control strategy, but only the scan rate adaptation component is replicated here for the comparison. Although it is not clear how the sample topography gradient necessary for the adaptation law is obtained in [27], the true sample gradient is known for Scenario One and is directly fed to the adaptation law. The parameters are chosen to be $\kappa = 1$, $\nabla h^* = 50$ and $d^* = 3$. The desired traversing speed \dot{x}^* is chosen to be $10 \mu\text{m/s}$ to achieve a similar scan duration for a fair comparison.

The result of the existing adaptation law is shown in the right column of Fig. 8. It can be seen that the adaptation law does not maintain the moving maximum of regulation error at the specified value, despite it taking slightly longer to finish the scan. Also, in contrast to the proposed adaptation law, it reacts immediately to regulation error changes, resulting in large fluctuations in the scan rate (bottom right of Fig. 8). This may impose heavy burdens on the XY actuators and controllers and worsen the XY tracking performance.

To more systematically compare the two adaptation laws, a series of simulations are conducted by varying e_z^* and \dot{x}^* , respectively. The steady-state maximum regulation error and scan duration are recorded for each simulation. The fixed-rate scan method is also conducted for benchmarking. The result is shown in Fig. 9. It can be seen that the proposed adaptation

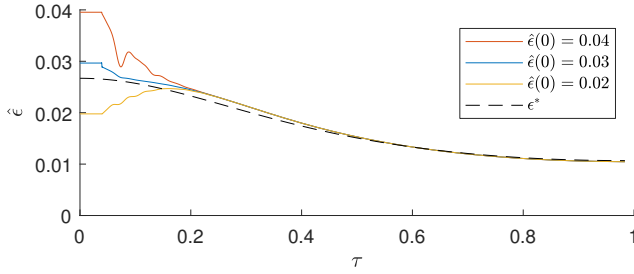


Fig. 5. Convergence of scan rate from different initial conditions under Scenario One.

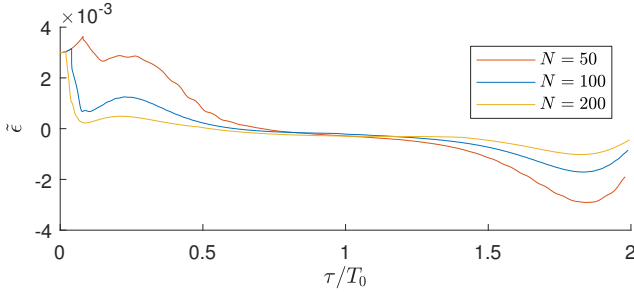


Fig. 6. Adaptation error reduces as N increases under Scenario One.

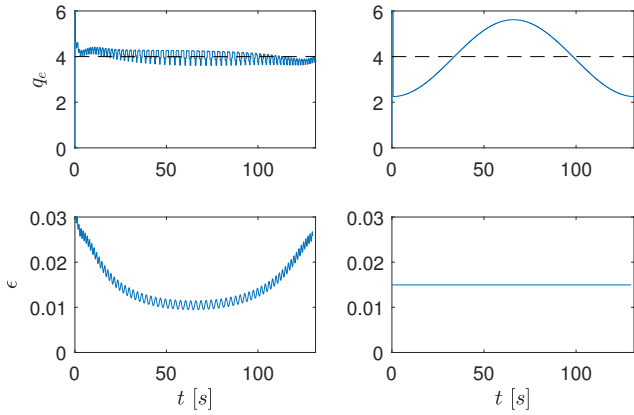


Fig. 7. Comparison between adaptive (left) and fixed-rate scan (right) under Scenario One.

law outperforms both fixed-rate scan method and the existing adaptation law. Furthermore, the existing adaptation law does not yield consistently better results than the fixed-rate scan. This is perhaps because such an ad-hoc algorithm does not necessarily lead to optimality.

C. Scenario Two: Periodic Rectangular Features and Spiral Scan

In order to demonstrate the generality of the proposed approach, another simulation study is conducted using a different scan pattern and different sample topography. In this scenario, a virtual NT-MDT TGZ1 calibration grating with periodic rectangular features of heights $h = 20$ nm is modelled with the superposition of 2D sigmoid functions (Fig. 4, right). Their shapes are tuned such that the generated regulation error are the same as that measured with the real TGZ1 sample. The

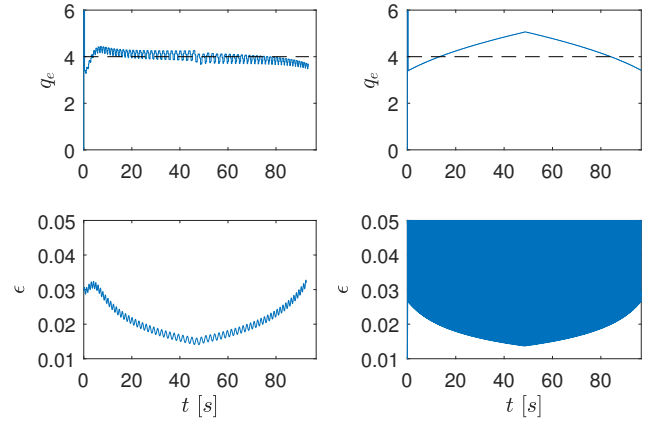


Fig. 8. Comparison between the proposed adaptive scan and the existing adaptive scan [27].

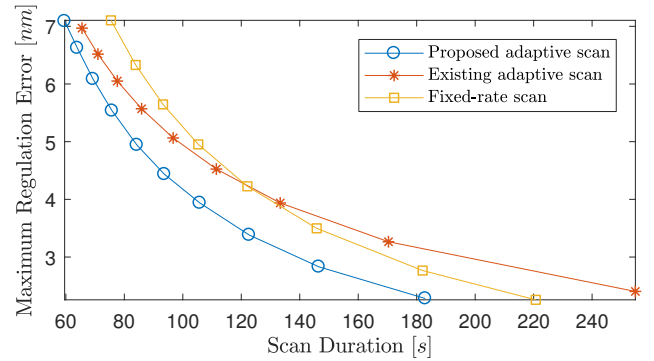


Fig. 9. Scan duration and maximum steady-state regulation error achieved by the proposed adaptive scan, existing adaptive scan [27], and fixed-rate scan.

spiral scan pattern described in Example 2 is applied with $L = 4 \mu\text{m}$ and $T_l = 0.01$ s, which implies a nominal scan duration of $T_0 = 1$ s for a 100-line scan.

The XY controller design is similar to the previous case except for the internal model. In particular, the stabilising controllers for both X and Y axes remain $D(s) = \frac{667}{s}$, and for each of the axes two internal modes are used in the form of Example 3 with $\omega_1 = \epsilon(\omega_l + \omega_{fs})$, $\omega_2 = \epsilon(\omega_l - \omega_{fs})$ and $\zeta_1 = \zeta_2 = 1$. The Z controller and the performance function remain the same. The ES parameters are also the same except now $\omega = 200$, $\delta = 0.5$. The optimiser remains inactive until $\tau = T_l + \frac{2\pi}{\omega}$.

It should be noted that in this scenario it is unlikely to obtain a closed-form expression of the steady-state cost map \bar{J} and optimal scan rate trajectory. However, it is known that the spiral scan generates a varying linear velocity which impacts on the bandwidth of the topography signal and hence on the imaging accuracy [38]. Therefore, it is expected that the scan rate would adapt accordingly to compensate for the variation in linear velocity. The simulation results confirm this. In Fig. 10, trajectories originating from three different initial conditions all converge to the same trajectory whose scan rate reduces as the scan progresses and spiral radius becomes larger. This is because the linear velocity in the centre is smaller than that at the edge of the scan. It may also be worth noting that the

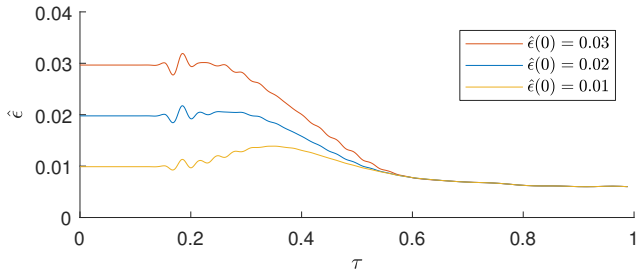


Fig. 10. Convergence of scan rate from different initial conditions under Scenario Two in simulation.

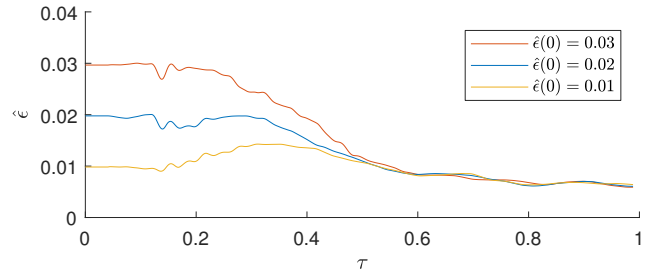


Fig. 14. Convergence of scan rate from different initial conditions under Scenario Two in experiment.

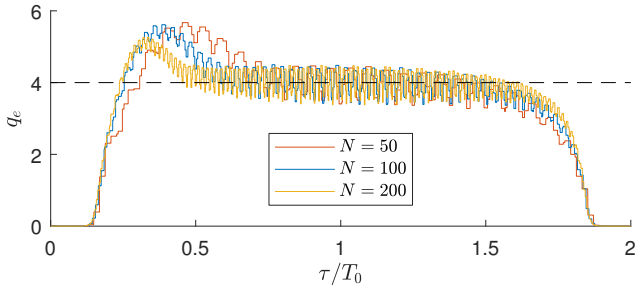


Fig. 11. Adaptation error reduces as N increases under Scenario Two in simulation.

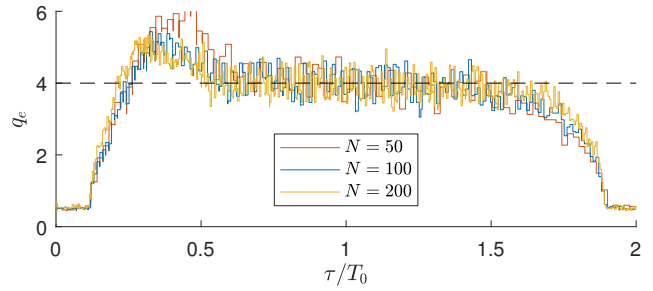


Fig. 15. Adaptation error reduces as N increases under Scenario Two in experiment.

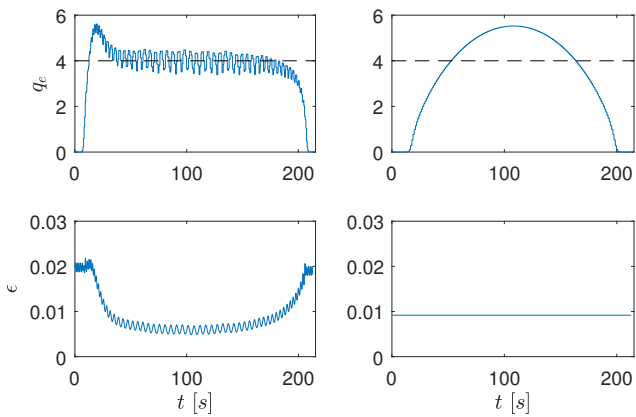


Fig. 12. Comparison between adaptive (left) and fixed-rate scan (right) under Scenario Two in simulation.

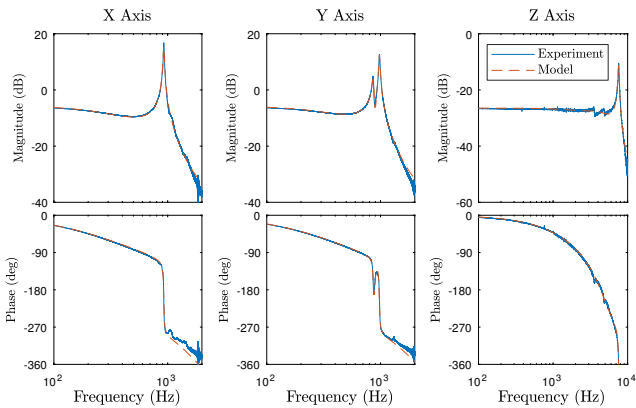
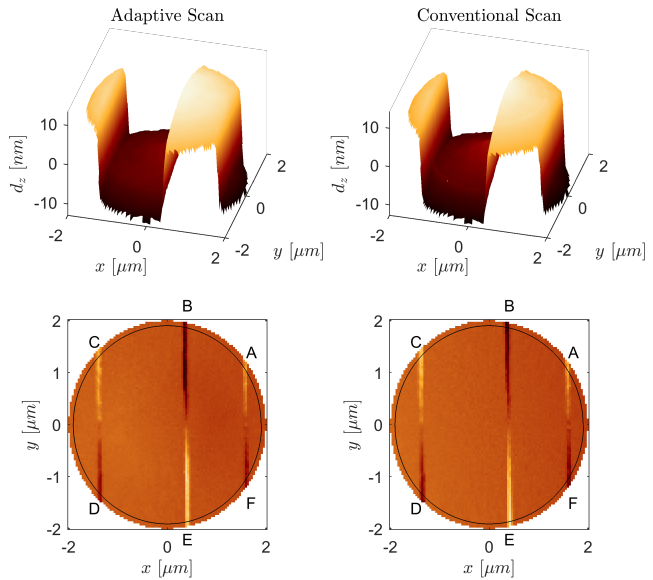


Fig. 13. System identification result.

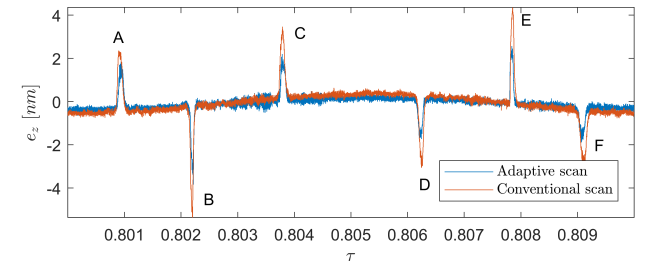


Fig. 16. Comparison between adaptive (left) and fixed-rate scan (right) under Scenario Two in experiment. From top to bottom: topography image, deflection image (regulation error), and error trajectory along one scan line indicated in the deflection image. The letters draw connections between features as shown in the deflection image and in the regulation error trajectory.

optimiser seems to be inactive for some period of time. This is due to the completely flat region at the centre of the scan where the gradient estimator fails to obtain a nonzero gradient.

Next, the effect of N on the adaptation is tested. Since the closed-form expression of the optimal scan trajectory is unavailable, instead of depicting the $\tilde{\epsilon}$ trajectory, Fig. 11 shows the trajectory of the maximum regulation error over the past scan line, $q_e(\tau) \triangleq \max_{\sigma \in [\tau - T_i, \tau]} |e_z(\sigma)|$. Three tests are performed with different choices of N , and each test consists of two consecutive scans (radially outward and inward). It can be seen that while q_e is kept around the set-point value in all three cases, the transient property improves as N increases.

Lastly, the adaptive scan method is again compared with the fixed-rate method. As shown in Fig. 12, it can be seen that except for some initial transient, the adaptive method manages to keep the regulation error at about the set-point value, whereas the fixed-rate method yields a varying error profile.

V. EXPERIMENT

A. Experimental Setup

The proposed extremum-seeking controller along with the XY trajectory generator and AFM image acquisition were implemented on a digital signal processing system (dSPACE MicroLabBox). The MicroLabBox is programmed using the Real-Time Interface for Simulink at a sample frequency of 10 kHz and software ControlDesk is used for the real-time application control. Higher sampling rates are possible, but not necessary due to the low XY closed-loop bandwidth (approximately 54 Hz). The analogue outputs of the MicroLabBox for commanding the XY nanopositioner of the AFM are amplified using a high-voltage amplifier (Nanonis HVA4) and connected to the signal access module of the AFM (NT-MDT NTEGRA) to directly control the internal piezoelectric tube actuator. Inbuilt capacitive sensors are used to measure the actuator displacements in X, Y and Z directions.

B. System Identification

System identification is performed by applying a low amplitude periodic chirp signal to the high-voltage amplifier and measuring the capacitive sensor outputs with complex averaging. Three different frequency ranges are measured to improve the signal-to-noise ratio for low frequencies. The high-voltage amplifier and capacitive sensors have a bandwidth of approximately 10 kHz. The measured frequency response functions (FRFs) along with the fitted models using subspace identification [39] are shown in Fig. 13. An internal time-delay in the NT-MDT AFM system is responsible for the phase roll-off. The three fitted transfer functions from high-voltage amplifier input to capacitive sensor output are (20)–(22). The bode plot for identified models are compared against the FRFs in Fig. 13. It can be seen that the identified plant dynamics well approximate the actual ones.

C. AFM Imaging

An NT-MDT TGZ1 calibration grating with periodic rectangular features of heights $h = 20 \pm 1.5$ nm is imaged in contact

mode using a spiral trajectory with a scan range of 4 μm (i.e. identical to Scenario Two in Section IV). The XY controller, performance function and ES parameters are designed as per Scenario Two and implemented in dSPACE. The inbuilt Z controller is used which generates a similar response to the one in simulation.

Overall, the results closely resemble those in simulation, although the responses are noisier due to ambient disturbances, sample contaminations and sensor measurement noise. In particular, Fig. 14 demonstrates the convergence to a steady state trajectory from various initial conditions and the convergence rates are very similar to those found in simulation (Fig. 10). Fig. 15 demonstrates that the desired imaging accuracy of 4 nm is achieved and the adaptation has better transient characteristics with a larger N . One may notice that the initial q_e is nonzero in contrast to the simulation. This is due to the nonzero Z sensor noise in the experiment.

Finally, Fig. 16 shows the comparison between AFM images for the adaptive and fixed-rate methods under $N = 100$ and the same duration. Although not shown here, the regulation error trajectories and scan rate trajectories are very close to the simulation results in Fig. 12. It can be seen that both methods generate similar topography images. In terms of the deflection image, which is a reflection of the regulation error signal, the adaptive method yields a more consistent magnitude of deflection, whereas that for the fixed-rate method increases along the radius. This is confirmed by the bottom figure which depicts the regulation error over the scan line indicated in the deflection image. Six regulation error peaks induced by the step features along the scan line are indicated by letters A–E. It can be seen that the adaptive method reduces the regulation error approximately by half towards the edge of the scan owing to the scan rate adaptation.

VI. CONCLUSION

An adaptive scan scheme based on the extremum-seeking control framework is proposed for AFM imaging. Under the proposed scheme, the scan rate is adapted online to achieve the best imaging performance in terms of imaging duration and accuracy as specified by the user. Under a few practical assumptions, it is shown that the scan rate converges to a neighbourhood of the optimal solution for a variety of scan patterns and performance measures. Example applications are provided for which the proposed scheme can achieve a more desirable imaging performance than the fixed-rate method.

APPENDIX

PROOF OF THEOREM 1

The proof resembles that of [29]. However, a notable difference is that the proof here deals with a time-varying cost function. First, the extremum-seeking scheme (18)–(19) is seen as a feedback interconnection between the \tilde{x} -dynamics and the $\tilde{\epsilon}$ -dynamics, and bounds on the solutions $\tilde{x}(\tau)$ and $\tilde{\epsilon}(\tau)$ are derived. To do this, Propositions 9–11 in [29] are replicated here as Propositions 1–3 with due modifications. Finally, the obtained bounds are exploited to prove the main

theorem using a small-gain argument. To start with, Propositions 1–3 are stated below and proofs are given.

Proposition 1: Suppose Assumptions 1–5 hold, then there exists a function $\beta_x \in \mathcal{KL}$ and for each $\rho_x, \rho_\epsilon > 0$ there exists a function $\gamma_{xC} \in \mathcal{K}$ such that for all $\sup_{\tau \geq 0} |\tilde{x}[\tau]| \leq \rho_x$, $\sup_{\tau \geq 0} |\tilde{\epsilon}[\tau]| \leq \rho_\epsilon$ and for all bounded values of $a, \omega, \delta > 0$ and $\underline{N} \geq \underline{N}$ the following bound holds for all $\tau \geq 0$:

$$|\tilde{x}(\tau)| \leq \max \{ \beta_x (|\tilde{x}(0)|, \tau), \gamma_{xC}(a\omega) \}. \quad (23)$$

Proposition 2: Suppose Assumptions 1–5 hold, then there exists a function $\beta_\epsilon \in \mathcal{KL}$ and for each $\rho_x, \rho_\epsilon > 0$ there exist functions $\gamma_{\epsilon x}, \gamma_{\epsilon C} \in \mathcal{K}$ such that for all $\sup_{\tau \geq 0} |\tilde{x}[\tau]| \leq \rho_x$, $\sup_{\tau \geq 0} |\tilde{\epsilon}[\tau]| \leq \rho_\epsilon$ and for all bounded values of $a, \omega, \delta > 0$ and $\underline{N} \geq \underline{N}$ the following bound holds for any $\tau^* \geq \tau_d$ and all $\tau \geq \tau^*$:

$$|\tilde{\epsilon}(\tau)| \leq \max \left\{ \beta_\epsilon (|\tilde{\epsilon}(\tau^*)|, a^2\omega\delta(\tau - \tau^*)), \right. \\ \left. \gamma_{\epsilon x} \left(\frac{1}{a} \sup_{\tau \geq \tau^*} |\tilde{x}[\tau]| \right), \gamma_{\epsilon C} \left(a + \omega + \delta + \frac{1}{a^2\omega\delta\underline{N}} \right) \right\}. \quad (24)$$

Proposition 3: Suppose Assumptions 1–5 hold, then for each $\rho_x, \rho_\epsilon > 0$ there exists a constant $c_\epsilon > 0$ such that for all $\sup_{\tau \geq 0} |\tilde{x}[\tau]| \leq \rho_x$, $\sup_{\tau \geq 0} |\tilde{\epsilon}[\tau]| \leq \rho_\epsilon$ and for all bounded values of $a, \omega, \delta > 0$ and $\underline{N} \geq \underline{N}$ the following bound holds for all $\tau \geq 0$:

$$|\tilde{\epsilon}(\tau)| \leq |\tilde{\epsilon}(0)| + \left(a\omega\delta + \frac{1}{\underline{N}} \right) c_\epsilon \tau. \quad (25)$$

A. Proof of Proposition 1

Using V_x in Assumption 3 as a Lyapunov function candidate for (19) yields

$$\frac{dV_x}{d\tau} \leq -\alpha_f (|\tilde{x}|) - \left(\frac{\partial V_x}{\partial \tilde{x}} \frac{\partial M}{\partial \epsilon} + \frac{\partial V_x}{\partial \epsilon} \right) \left(\frac{d\hat{\epsilon}}{d\tau} + a\omega \cos(\omega\tau) \right).$$

Recall that $\hat{\epsilon}(\tau) = \tilde{\epsilon}(\tau) + \epsilon^*(N, \tau)$ and

$$\frac{d\hat{\epsilon}}{d\tau} = \frac{a\omega^2\delta}{\pi} \int_{\tau - \frac{2\pi}{\omega}}^{\tau} J(\tilde{x}[\sigma], \xi_r[\sigma], \epsilon[\sigma], N) s(\sigma) d\sigma.$$

It can be seen that, given bounded values of $a, \omega, \delta, \frac{1}{\underline{N}} > 0$ and uniformly bounded trajectories of $\tilde{x}(\tau), \tilde{\epsilon}(\tau), \epsilon^*(N, \tau)$ for all $\tau \geq -\tau_d$, there exists some constant $c_{J1} > 0$ such that

$$|J(\tilde{x}[\sigma], \xi_r[\sigma], \epsilon[\sigma], N) s(\sigma)| \leq c_{J1}$$

for all $\sigma \geq -\frac{2\pi}{\omega}$ and therefore

$$\left| \frac{d\hat{\epsilon}}{d\tau} \right| \leq 2a\omega\delta c_{J1}$$

for $\tau \geq 0$. Thus, it can be seen that there exists some $C_x > 0$ such that

$$\frac{dV_x}{d\tau} \leq -\alpha_f (|\tilde{x}|) + a\omega C_x.$$

Then it follows that

$$\frac{dV_x}{d\tau} \leq -\frac{1}{2}\alpha_f (|\tilde{x}|)$$

when

$$|\tilde{x}| \geq \alpha_f^{-1} (2a\omega C_x).$$

Therefore, using Theorem 4.18 in [40], it can be shown that Proposition 1 holds with $\gamma_{xC}(\sigma) \triangleq \alpha_{x1}^{-1} \circ \alpha_{x2} \circ \alpha_f^{-1} (2C_x\sigma)$.

B. Proof of Proposition 2

First rewrite (19) as

$$\frac{d\tilde{\epsilon}}{d\tau} = a^2\omega\delta \frac{\partial \bar{J}}{\partial \epsilon} (\hat{\epsilon}(\tau), N, \tau) + a\omega\delta\Delta_1 + a\omega\delta\Delta_2 \\ + a\omega\delta\Delta_3 + a\omega\delta\Delta_4 - \frac{\partial \epsilon^*}{\partial \tau} (N, \tau)$$

with

$$\Delta_1 \triangleq \frac{\omega}{\pi} \int_{\tau - \frac{2\pi}{\omega}}^{\tau} (\bar{J}(\hat{\epsilon}(\sigma) + as(\sigma), N, \sigma) \\ - \bar{J}(\hat{\epsilon}(\tau) + as(\tau), N, \tau)) s(\sigma) d\sigma,$$

$$\Delta_2 \triangleq \frac{\omega}{\pi} \int_{\tau - \frac{2\pi}{\omega}}^{\tau} (J(0, \xi_r[\sigma], \epsilon[\sigma], N) \\ - \bar{J}(\hat{\epsilon}(\sigma) + as(\sigma), N, \sigma)) s(\sigma) d\sigma,$$

$$\Delta_3 \triangleq \frac{\omega}{\pi} \int_{\tau - \frac{2\pi}{\omega}}^{\tau} (J(\tilde{x}[\sigma], \xi_r[\sigma], \epsilon[\sigma], N) \\ - J(0, \xi_r[\sigma], \epsilon[\sigma], N)) s(\sigma) d\sigma,$$

$$\Delta_4 \triangleq \frac{\omega}{\pi} \int_{\tau - \frac{2\pi}{\omega}}^{\tau} R(\tau, \sigma) s(\sigma) d\sigma,$$

where $R(\tau, \sigma)$ is the remainder term after Taylor expansion which has the expression of $R(\tau, \sigma) \triangleq a^2s^2(\sigma) \int_0^1 (1-r) \frac{\partial^2 \bar{J}}{\partial \epsilon^2} (\hat{\epsilon}(\tau) + as(\sigma)r, N, \tau) dr$.

For $|\Delta_1|$, notice that

$$\bar{J}(\hat{\epsilon}(\sigma) + as(\sigma), N, \sigma) - \bar{J}(\hat{\epsilon}(\tau) + as(\tau), N, \tau) \\ = \int_{\tau}^{\sigma} \left(\frac{\partial \bar{J}}{\partial \epsilon} (\hat{\epsilon}(r) + as(\sigma), N, r) \frac{d\hat{\epsilon}}{d\tau}(r) \right. \\ \left. + \frac{\partial \bar{J}}{\partial \tau} (\hat{\epsilon}(r) + as(\sigma), N, r) \right) dr$$

for all $\sigma \in [\tau - \frac{2\pi}{\omega}, \tau]$ and all $\tau \geq \frac{2\pi}{\omega}$. Using a result from the Proof of Proposition 1, it can be seen that there exists some constant $c_{J2} > 0$ such that

$$\left| \frac{d\hat{\epsilon}}{d\tau}(r) \right| \leq a\omega\delta c_{J2}$$

for $r \geq 0$. Moreover, by Assumption 5,

$$\left| \frac{\partial \bar{J}}{\partial \tau} (\hat{\epsilon}(r) + as(\sigma), N, r) \right| \leq \frac{k_J}{\underline{N}}$$

for $r \geq 0$. Therefore, it can be seen that there exists some constant $C_{\Delta_1} > 0$ such that

$$|\Delta_1| \leq \left(a\delta + \frac{1}{\omega\underline{N}} \right) C_{\Delta_1}$$

for all $\tau \geq \frac{2\pi}{\omega}$.

For $|\Delta_2|$, for each $\sigma \in [\tau - \frac{2\pi}{\omega}, \tau]$ where $\tau \in \mathbb{R}$, define $\epsilon_1[\sigma], \epsilon_2[\sigma] \in \mathcal{C}([-\tau_d, 0]; \mathcal{Q})$ where $\mathcal{Q} \subset \mathbb{R}$ is a compact set, recall the definition of J and note (12), and then it could be seen that

$$|J(0, \xi_r[\sigma], \epsilon_1[\sigma], N) - J(0, \xi_r[\sigma], \epsilon_2[\sigma], N)| \\ \leq |g_e \circ L_e \circ \bar{e}_{z1}[\sigma] - g_e \circ L_e \circ \bar{e}_{z2}[\sigma]| \\ + |g_s \circ L_s \circ \epsilon_1[\sigma] - g_s \circ L_s \circ \epsilon_2[\sigma]|,$$

where $\bar{e}_{z1}[\sigma] \triangleq h_z \circ M(\xi_r[\sigma], \epsilon_1[\sigma], N)$ and $\bar{e}_{z2}[\sigma] \triangleq h_z \circ M(\xi_r[\sigma], \epsilon_2[\sigma], N)$. Notice the facts that $L_e \circ \bar{e}_{z1}[\sigma] - L_e \circ \bar{e}_{z2}[\sigma] \leq \max_{r \in [-T_l, 0]} |\bar{e}_{z1}(\sigma + r) - \bar{e}_{z2}(\sigma + r)|$ by the definition of L_e in (13) and that $L_s \circ \epsilon_1[\sigma] - L_s \circ \epsilon_2[\sigma] \leq \max_{r \in [-T_l, 0]} |\epsilon_1(\sigma + r) - \epsilon_2(\sigma + r)|$ for $\tau_\phi \leq T_l$ by the definition of L_s (14). Then, due to the smoothness of g_e , g_s , h_z and M , it can be seen that there exists $C_M > 0$ such that

$$\begin{aligned} & |J(0, \xi_r[\sigma], \epsilon_1[\sigma], N) - J(0, \xi_r[\sigma], \epsilon_2[\sigma], N)| \\ & \leq C_M \max_{r \in [-T_l, 0]} |\epsilon_1(\sigma + r) - \epsilon_2(\sigma + r)|. \end{aligned}$$

Now, for each $\sigma \in [\tau - \frac{2\pi}{\omega}, \tau]$ where $\tau \geq -T_l$, define $\bar{e}_\sigma(r) = \hat{e}(\sigma) + as(\sigma)$ for all $r \in \mathbb{R}$, then by definition $\bar{J}(\hat{e}(\sigma) + as(\sigma), N, \sigma) = J(0, \xi_r[\sigma], \bar{e}_\sigma[\sigma], N)$. Also, since by assumption $\tilde{\epsilon}[\sigma], \epsilon^*[N, \sigma] \in \mathcal{C}([- \tau_d, 0]; \mathcal{Q})$, it can be seen that $\epsilon[\sigma], \bar{e}_\sigma[\sigma] \in \mathcal{C}([- \tau_d, 0]; \mathcal{Q})$ as well. Therefore,

$$\begin{aligned} & |J(0, \xi_r[\sigma], \epsilon[\sigma], N) - \bar{J}(\hat{e}(\sigma) + as(\sigma), N, \sigma)| \\ & = |J(0, \xi_r[\sigma], \epsilon[\sigma], N) - J(0, \xi_r[\sigma], \bar{e}_\sigma[\sigma], N)| \\ & \leq C_M \max_{r \in [-T_l, 0]} |\epsilon(\sigma + r) - \bar{e}_\sigma(\sigma + r)| \\ & = C_M \max_{r \in [-T_l, 0]} |\epsilon(\sigma + r) - \hat{e}(\sigma) - as(\sigma)| \\ & \leq C_M \max_{r \in [-T_l, 0]} |\hat{e}(\sigma + r) - \hat{e}(\sigma)| \\ & \quad + C_M \max_{r \in [-T_l, 0]} |a \sin(\omega(\sigma + r)) - a \sin(\omega(\sigma - \tau_\phi))| \end{aligned}$$

for all $\sigma \in [\tau - \frac{2\pi}{\omega}, \tau]$ where $\tau \geq 0$. Notice that

$$\begin{aligned} & \max_{r \in [-T_l, 0]} |\hat{e}(\sigma + r) - \hat{e}(\sigma)| \\ & \leq T_l \max_{r \in [\sigma - T_l, \sigma]} \left| \frac{d\hat{e}}{d\tau}(r) \right| \\ & \leq a\omega\delta T_l c_{J2} \end{aligned}$$

holds for all $\sigma \in [\tau - \frac{2\pi}{\omega}, \tau]$ where $\tau \geq \tau_d$, and

$$\begin{aligned} & \max_{r \in [-T_l, 0]} |a \sin(\omega(\sigma + r)) - a \sin(\omega(\sigma - \tau_\phi))| \\ & = \max_{r \in [-T_l, 0]} \left| \int_{\sigma - \tau_\phi}^{\sigma + r} a\omega \cos(\omega\rho) d\rho \right| \\ & \leq a\omega \max_{r \in [-T_l, 0]} |r - \tau_\phi| \end{aligned}$$

holds for all $\sigma \in [\tau - \frac{2\pi}{\omega}, \tau]$ where $\tau \in \mathbb{R}$. Therefore, it follows that there exists some constant $C_{\Delta_2} > 0$ such that

$$|\Delta_2| \leq a\omega C_{\Delta_2}$$

for all $\tau \geq \tau_d$.

For $|\Delta_3|$, using a similar analysis as before, it could be seen that for each $\sigma \in [\tau - \frac{2\pi}{\omega}, \tau]$ where $\tau \geq 0$,

$$\begin{aligned} & |J(\tilde{x}[\sigma], \xi_r[\sigma], \epsilon[\sigma], N) - J(0, \xi_r[\sigma], \epsilon[\sigma], N)| \\ & = |g_e \circ L_e \circ h_z(\tilde{x}[\sigma] + M(\xi_r[\sigma], \epsilon[\sigma], N)) \\ & \quad - g_e \circ L_e \circ h_z(M(\xi_r[\sigma], \epsilon[\sigma], N))| \\ & \leq C_J \max_{r \in [-T_l, 0]} |\tilde{x}(\sigma + r)|. \end{aligned}$$

Therefore, it follows that there exists some constant $C_{\Delta_3} > 0$ such that

$$|\Delta_3| \leq C_{\Delta_3} |\tilde{x}[\tau]|$$

for all $\tau \geq 0$.

For $|\Delta_4|$, since by Assumption 4 $\frac{\partial^2 \bar{J}}{\partial \epsilon^2}$ is bounded for bounded trajectories of $\tilde{\epsilon}(\tau), \epsilon^*(N, \tau)$ for all $\sigma \in [\tau - \frac{2\pi}{\omega}, \tau]$ and $\tau \geq -\tau_d$, it follows that there exists some constant $C_{\Delta_4} > 0$ such that

$$|\Delta_4| \leq a^2 C_{\Delta_4}$$

for all $\tau \geq -\tau_d$.

Lastly, by Assumption 5,

$$\left| \frac{\partial \epsilon^*}{\partial \tau} \right| \leq \frac{k_\epsilon}{N}$$

for $\tau \geq 0$.

Now, using the Lyapunov-Razumikhin function candidate $V_\epsilon(\tilde{\epsilon}) \triangleq \frac{\tilde{\epsilon}^2}{2}$, it follows that

$$\begin{aligned} \frac{dV_\epsilon}{d\tau} & = a^2 \omega \delta \frac{\partial \bar{J}}{\partial \epsilon}(\hat{e}(\tau), N, \tau) \tilde{\epsilon} + a\omega \delta \Delta_1 \tilde{\epsilon} + a\omega \delta \Delta_2 \tilde{\epsilon} \\ & \quad + a\omega \delta \Delta_3 \tilde{\epsilon} + a\omega \delta \Delta_4 \tilde{\epsilon} - \frac{\partial \epsilon^*}{\partial \tau}(N, \tau) \tilde{\epsilon}. \end{aligned}$$

Substituting the obtained upper bounds into the equation while noting $|\tilde{\epsilon}| \leq \rho_\epsilon$ yields

$$\begin{aligned} \frac{dV_\epsilon}{d\tau} & \leq -a^2 \omega \delta \left(\alpha_J(|\tilde{\epsilon}|) - \delta C_{\Delta_1} \rho_\epsilon - \omega C_{\Delta_2} \rho_\epsilon \right. \\ & \quad \left. - \frac{1}{a} C_{\Delta_3} |\tilde{x}[\tau]| \rho_\epsilon - a C_{\Delta_4} \rho_\epsilon - \frac{a \delta C_{\Delta_1} + k_\epsilon}{a^2 \omega \delta N} \rho_\epsilon \right) \\ & \leq -a^2 \omega \delta \left(\alpha_J(|\tilde{\epsilon}|) - \left(\delta + \omega + a + \frac{1}{a^2 \omega \delta N} \right) C_\epsilon \rho_\epsilon \right. \\ & \quad \left. - \frac{1}{a} C_{\Delta_3} \rho_\epsilon |\tilde{x}[\tau]| \right) \end{aligned}$$

for some $C_\epsilon > 0$. Then, provided that

$$|\tilde{\epsilon}| \geq \alpha_J^{-1} \left(4 \left(\delta + \omega + a + \frac{1}{a^2 \omega \delta N} \right) C_\epsilon \rho_\epsilon \right)$$

and

$$|\tilde{\epsilon}| \geq \alpha_J^{-1} \left(\frac{4}{a} C_{\Delta_3} \rho_\epsilon |\tilde{x}[\tau]| \right),$$

it follows that

$$\frac{dV_\epsilon}{d\tau} \leq -\frac{1}{2} a^2 \omega \delta \alpha_J(|\tilde{\epsilon}|)$$

for $\tau \geq \tau_d$. Therefore, using an analysis that is similar to Theorem 4.19 in [40], it can be shown that Proposition 2 holds with $\gamma_{\epsilon x}(\sigma) \triangleq \alpha_J^{-1}(4C_{\Delta_3} \rho_\epsilon \sigma)$ and $\gamma_{\epsilon C}(\sigma) \triangleq \alpha_J^{-1}(4C_\epsilon \rho_\epsilon \sigma)$.

C. Proof of Proposition 3

Recall that $\frac{d\tilde{\epsilon}}{d\tau} = \frac{d\hat{e}}{d\tau} - \frac{\partial \epsilon^*}{\partial \tau}$ and using a result from the Proof of Proposition 1, it can be seen that there exists some constant $c_{J3} > 0$ such that

$$\left| \frac{d\hat{e}}{d\tau} \right| \leq 2a\omega \delta c_{J3}$$

for $\tau \geq 0$. Moreover, by Assumption 5,

$$\left| \frac{\partial \epsilon^*}{\partial \tau} \right| \leq \frac{k_\epsilon}{N}$$

for $\tau \geq 0$. Then it follows that

$$\begin{aligned} \left| \frac{d\tilde{\epsilon}}{d\tau} \right| &\leq 2a\omega\delta c_{J3} + \frac{k_\epsilon}{N} \\ &\leq \left(a\omega\delta + \frac{1}{N} \right) c_\epsilon \end{aligned}$$

for all $\tau \geq 0$ for $c_\epsilon \triangleq \max\{2c_{J3}, k_\epsilon\}$. Therefore,

$$|\tilde{\epsilon}(\tau)| \leq |\tilde{\epsilon}(0)| + \left(a\omega\delta + \frac{1}{N} \right) c_\epsilon \tau$$

for all $\tau \geq 0$.

D. Proof of Main Theorem

Assume without loss of generality that $\nu_\epsilon < \min\{\rho_\epsilon^0, \underline{\epsilon}^*, \bar{\epsilon} - \bar{\epsilon}^*\}$ where $\underline{\epsilon}^*$ and $\bar{\epsilon}^*$ are introduced in Assumption 4. Choose $\rho_x, \rho_\epsilon > 0$ in Propositions 1–3 to be

$$\begin{aligned} \rho_x &> \beta_x(\rho_x^0, 0), \\ \rho_\epsilon &> \beta_\epsilon(\rho_\epsilon^0 + \rho_\epsilon^+, 0), \end{aligned}$$

where $\beta_x, \beta_\epsilon \in \mathcal{KL}$ are defined in Proposition 1 and 2 respectively, and $\rho_\epsilon^+ \in (0, \nu_\epsilon^+)$ is arbitrary. It is also assumed without loss of generality that $\beta_x(\sigma, 0) \geq \sigma$ and $\beta_\epsilon(\sigma, 0) \geq \sigma$ for all $\sigma \geq 0$. Now, recall c_ϵ in Proposition 3 and k_ϵ in Assumption 5, and let $a^* = \min\{\gamma_{\epsilon C}^{-1}(\min\{\rho_\epsilon, \nu_\epsilon\}), \nu_\epsilon^+ - \rho_\epsilon^+, \underline{\epsilon}^* - \nu_\epsilon, \bar{\epsilon} - \bar{\epsilon}^* - \nu_\epsilon\}$, then for any $a \in (0, a^*)$, let $\omega^* = \min\{\gamma_{\epsilon C}^{-1}(\min\{\rho_\epsilon, \nu_\epsilon\}) - a, \frac{1}{a}\gamma_{x C}^{-1}(\min\{\rho_x, \nu_x\}), \frac{1}{a}\gamma_{x C}^{-1}(a\gamma_{\epsilon x}(\min\{\rho_\epsilon, \nu_\epsilon\}))\}$, then for any $\omega \in (0, \omega^*)$, let τ_0^* be such that $\beta_x(\rho_x^0, \tau_0^* - \tau_d) = a\gamma_{\epsilon x}^{-1}(\min\{\rho_\epsilon, \nu_\epsilon\})$, then for any $\tau^* > \tau_0^*$, let $\delta^* = \min\{\gamma_{\epsilon C}^{-1}(\min\{\rho_\epsilon, \nu_\epsilon\}) - a - \omega, \frac{\rho_\epsilon^+}{c_\epsilon \tau^* a \omega}\}$, then for any $\delta \in (0, \delta^*)$, let τ^{**} be such that $\beta_\epsilon(\rho_\epsilon^0 + \rho_\epsilon^+, a^2\omega\delta\tau^{**}) = \nu_\epsilon$, and let $N^* = \max\left\{\frac{1}{a^2\omega\delta(\gamma_{\epsilon C}^{-1}(\min\{\rho_\epsilon, \nu_\epsilon\}) - a - \omega - \delta)}, \frac{1}{\frac{\rho_\epsilon^+}{c_\epsilon \tau^*} - a\omega\delta}, \frac{k_\epsilon(\tau^* + \tau^{**})}{\nu_\epsilon^+ - \rho_\epsilon^+ - a}\right\}$, then for any $N > N^*$, it can be shown that the following inequalities hold:

$$a\omega < \gamma_{x C}^{-1}(\rho_x), \quad (26)$$

$$a\omega < \gamma_{x C}^{-1}(a\gamma_{\epsilon x}^{-1}(\rho_\epsilon)), \quad (27)$$

$$\beta_x(\rho_x^0, \tau^* - \tau_d) < a\gamma_{\epsilon x}^{-1}(\rho_\epsilon), \quad (28)$$

$$a + \omega + \delta + \frac{1}{a^2\omega\delta N} < \gamma_{\epsilon C}^{-1}(\rho_\epsilon), \quad (29)$$

$$a\omega\delta + \frac{1}{N} < \frac{\rho_\epsilon^+}{c_\epsilon \tau^*}, \quad (30)$$

$$a\omega < \gamma_{x C}^{-1}(\nu_x), \quad (31)$$

$$a\omega < \gamma_{x C}^{-1}(a\gamma_{\epsilon x}^{-1}(\nu_\epsilon)), \quad (32)$$

$$\beta_x(\rho_x^0, \tau^* - \tau_d) < a\gamma_{\epsilon x}^{-1}(\nu_\epsilon), \quad (33)$$

$$a + \omega + \delta + \frac{1}{a^2\omega\delta N} < \gamma_{\epsilon C}^{-1}(\nu_\epsilon), \quad (34)$$

$$\frac{k_\epsilon}{N} < \frac{\nu_\epsilon^+ - \rho_\epsilon^+ - a}{\tau^* + \tau^{**}}. \quad (35)$$

It can be firstly proved by contradiction that the bounds on the system solution required by Propositions 1–3 indeed hold, i.e. $\sup_{\tau \geq 0} |\tilde{x}[\tau]| \leq \rho_x$ and $\sup_{\tau \geq 0} |\tilde{\epsilon}[\tau]| \leq \rho_\epsilon$. Suppose it does

not and there exists $\tau_2 > 0$ such that either $|\tilde{x}(\tau_2)| > \rho_x$ or $|\tilde{\epsilon}(\tau_2)| > \rho_\epsilon$. Due to the continuity of the solution, and notice that $|\tilde{x}(0)| \leq \rho_x^0 < \rho_x$ and $|\tilde{\epsilon}(0)| \leq \rho_\epsilon^0 < \rho_\epsilon$, there must exist $\tau_1 > 0$ such that

$$|\tilde{x}(\tau_1)| = \rho_x \text{ or } |\tilde{\epsilon}(\tau_1)| = \rho_\epsilon \quad (36)$$

but

$$\sup_{\tau \in [0, \tau_1]} |\tilde{x}[\tau]| \leq \rho_x \text{ and } \sup_{\tau \in [0, \tau_1]} |\tilde{\epsilon}[\tau]| \leq \rho_\epsilon.$$

However, it should be noted that (23)–(25) are still valid for $\tau \in [0, \tau_1]$ due to causality. Therefore, using (23)–(30) it can be shown that the system solution satisfies

$$\sup_{\tau \in [0, \tau_1]} |\tilde{x}[\tau]| < \rho_x \text{ and } \sup_{\tau \in [0, \tau_1]} |\tilde{\epsilon}[\tau]| < \rho_\epsilon,$$

which contradicts (36). Therefore, the bounds $\sup_{\tau \geq 0} |\tilde{x}[\tau]| \leq \rho_x$ and $\sup_{\tau \geq 0} |\tilde{\epsilon}[\tau]| \leq \rho_\epsilon$ for Propositions 1–3 must hold. Next, using (23)–(25) and (31)–(34) it can be shown that

$$\limsup_{\tau \rightarrow \infty} \begin{bmatrix} |\tilde{x}(\tau)| \\ |\tilde{\epsilon}(\tau)| \end{bmatrix} \leq \begin{bmatrix} \nu_x \\ \nu_\epsilon \end{bmatrix}.$$

Finally, the rest of the proof is to show that

$$0 < \epsilon(\tau) < \bar{\epsilon}$$

for all $\tau \geq 0$. Noting $\nu_\epsilon^+ \leq \hat{\epsilon}(0) \leq \bar{\epsilon} - \nu_\epsilon^+$, it can be seen that

$$\nu_\epsilon^+ - \epsilon^*(N, 0) \leq \tilde{\epsilon}(0) \leq \bar{\epsilon} - \nu_\epsilon^+ - \epsilon^*(N, 0).$$

Using a result from the Proof of Proposition 3 and (30), it can be shown that

$$|\tilde{\epsilon}(\tau) - \tilde{\epsilon}(0)| \leq \rho_\epsilon^+$$

and therefore

$$\nu_\epsilon^+ - \rho_\epsilon^+ - \epsilon^*(N, 0) \leq \tilde{\epsilon}(\tau) \leq \bar{\epsilon} - \nu_\epsilon^+ + \rho_\epsilon^+ - \epsilon^*(N, 0)$$

for $0 \leq \tau \leq \tau^*$. Since $\tilde{\epsilon}$ is a scalar variable, $\tilde{\epsilon}(\tau)$ converges monotonically towards the ball of radius ν_ϵ for $\tau \geq \tau^*$ and stays inside the ball for $\tau \geq \tau^* + \tau^{**}$. Therefore,

$$\nu_\epsilon^+ - \rho_\epsilon^+ - \epsilon^*(N, 0) \leq \tilde{\epsilon}(\tau) \leq \bar{\epsilon} - \nu_\epsilon^+ + \rho_\epsilon^+ - \epsilon^*(N, 0)$$

for $\tau^* \leq \tau \leq \tau^* + \tau^{**}$ and

$$|\tilde{\epsilon}(\tau)| \leq \nu_\epsilon$$

for $\tau \geq \tau^* + \tau^{**}$. Then, noting $\epsilon(\tau) = \tilde{\epsilon}(\tau) + \epsilon^*(N, \tau) + a \sin(\omega\tau)$,

$$\left| \frac{\partial \epsilon^*}{\partial \tau} \right| \leq \frac{k_\epsilon}{N}$$

by Assumption 5, and (35), it can be seen that

$$\begin{aligned} \epsilon(\tau) &\geq \nu_\epsilon^+ - \rho_\epsilon^+ - \frac{k_\epsilon}{N}(\tau^* + \tau^{**}) - a \\ &> \nu_\epsilon^+ - \rho_\epsilon^+ - (\nu_\epsilon^+ - \rho_\epsilon^+ - a) - a \\ &= 0 \end{aligned}$$

and

$$\begin{aligned} \epsilon(\tau) &\leq \bar{\epsilon} - \nu_\epsilon^+ + \rho_\epsilon^+ + \frac{k_\epsilon}{N}(\tau^* + \tau^{**}) + a \\ &< \bar{\epsilon} - \nu_\epsilon^+ + \rho_\epsilon^+ + (\nu_\epsilon^+ - \rho_\epsilon^+ - a) + a \\ &= \bar{\epsilon} \end{aligned}$$

for $0 \leq \tau \leq \tau^* + \tau^{**}$, and

$$\begin{aligned} \epsilon(\tau) &\geq -\nu_\epsilon + \underline{\epsilon}^* - a \\ &> 0 \end{aligned}$$

and

$$\begin{aligned} \epsilon(\tau) &\leq \nu_\epsilon + \bar{\epsilon}^* + a \\ &< \bar{\epsilon} \end{aligned}$$

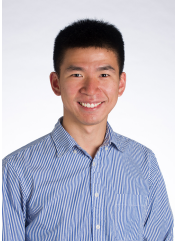
for $\tau \geq \tau^* + \tau^{**}$. It follows that

$$0 < \epsilon(\tau) < \bar{\epsilon}$$

for all $\tau \geq 0$, and the theorem is proved.

REFERENCES

- [1] N. C. Santos and M. A. R. B. Castanho, "An overview of the biophysical applications of atomic force microscopy," *Biophysical Chemistry*, vol. 107, no. 2, pp. 133–149, 2004.
- [2] L. Gross, F. Mohn, N. Moll, P. Liljeroth, and G. Meyer, "The chemical structure of a molecule resolved by atomic force microscopy," *Science*, vol. 325, no. 5944, pp. 1110–1114, 2009.
- [3] D. Y. Abramovitch, S. B. Andersson, L. Y. Pao, and G. Schitter, "A tutorial on the mechanisms, dynamics, and control of atomic force microscopes," in *American Control Conference, 2007. ACC'07.* IEEE, 2007, pp. 3488–3502.
- [4] A. J. Fleming, B. J. Kenton, and K. K. Leang, "Bridging the gap between conventional and video-speed scanning probe microscopes," *Ultramicroscopy*, vol. 110, no. 9, pp. 1205–1214, 2010.
- [5] A. Sebastian and S. M. Salapaka, "Design methodologies for robust nano-positioning," *IEEE Transactions on Control Systems Technology*, vol. 13, no. 6, pp. 868–876, 2005.
- [6] K. K. Leang and S. Devasia, "Feedback-linearized inverse feedforward for creep, hysteresis, and vibration compensation in AFM piezoactuators," *IEEE Transactions on Control Systems Technology*, vol. 15, no. 5, pp. 927–935, 2007.
- [7] A. Esbrook, X. Tan, and H. K. Khalil, "Control of systems with hysteresis via servocompensation and its application to nanopositioning," *IEEE Transactions on Control Systems Technology*, vol. 21, no. 3, pp. 725–738, 2013.
- [8] S. K. Das, H. R. Pota, and I. R. Petersen, "Resonant controller design for a piezoelectric tube scanner: A mixed negative-imaginary and small-gain approach," *IEEE Transactions on Control Systems Technology*, vol. 22, no. 5, pp. 1899–1906, 2014.
- [9] S. Devasia, E. Eleftheriou, and S. R. Moheimani, "A survey of control issues in nanopositioning," *IEEE Transactions on Control Systems Technology*, vol. 15, no. 5, pp. 802–823, 2007.
- [10] Y. K. Yong, S. O. R. Moheimani, and I. R. Petersen, "High-speed cycloid-scan atomic force microscopy," *Nanotechnology*, vol. 21, no. 36, p. 365503, 2010.
- [11] I. A. Mahmood, S. O. R. Moheimani, and B. Bhikkaji, "A new scanning method for fast atomic force microscopy," *IEEE Transactions on Nanotechnology*, vol. 10, no. 2, pp. 203–216, 2011.
- [12] A. Bazaeei, Y. K. Yong, and S. O. R. Moheimani, "High-speed Lissajous-scan atomic force microscopy: Scan pattern planning and control design issues," *Review of Scientific Instruments*, vol. 83, no. 6, p. 63701, 2012.
- [13] Y. K. Yong, A. Bazaeei, and S. O. R. Moheimani, "Video-rate Lissajous-scan atomic force microscopy," *IEEE Transactions on Nanotechnology*, vol. 13, no. 1, pp. 85–93, 2014.
- [14] A. Bazaeei, Y. K. Yong, and S. R. Moheimani, "Combining spiral scanning and internal model control for sequential afm imaging at video rate," *IEEE/ASME Transactions on Mechatronics*, vol. 22, no. 1, pp. 371–380, 2017.
- [15] J. A. Butterworth, L. Y. Pao, and D. Y. Abramovitch, "A discrete-time single-parameter combined feedforward/feedback adaptive-delay algorithm with applications to piezo-based raster tracking," *IEEE Transactions on Control Systems Technology*, vol. 20, no. 2, pp. 416–423, 2012.
- [16] M. Kara-Mohamed, W. P. Heath, and A. Lanzon, "Enhanced Tracking for Nanopositioning Systems Using Feedforward/Feedback Multivariable Control Design," *IEEE Transactions on Control Systems Technology*, vol. 23, no. 3, pp. 1003–1013, 2015.
- [17] K. Wang, C. Manzie, and D. Nešić, "A framework for reference generation and control in afm imaging," in *Control Conference (AuCC), 2016 Australian.* IEEE, 2016, pp. 288–293.
- [18] A. J. Fleming, "Dual-stage vertical feedback for high-speed scanning probe microscopy," *IEEE Transactions on Control Systems Technology*, vol. 19, no. 1, pp. 156–165, 2011.
- [19] S. Kuiper and G. Schitter, "Model-based feedback controller design for dual actuated atomic force microscopy," *Mechatronics*, vol. 22, no. 3, pp. 327–337, 2012.
- [20] Y. K. Yong and S. O. R. Moheimani, "Design of an inertially counterbalanced Z-nanopositioner for high-speed atomic force microscopy," *IEEE Transactions on Nanotechnology*, vol. 12, no. 2, pp. 137–145, 2013.
- [21] G. Schitter, P. Menold, H. F. Knapp, F. Allgöwer, and A. Stemmer, "High performance feedback for fast scanning atomic force microscopes," *Review of Scientific Instruments*, vol. 72, no. 8, pp. 3320–3327, 2001.
- [22] J. Ren and Q. Zou, "High-speed adaptive contact-mode atomic force microscopy imaging with near-minimum-force," *Review of Scientific Instruments*, vol. 85, no. 7, p. 073706, 2014.
- [23] S. Necipoglu, S. Cebeci, Y. E. Has, L. Guvenc, and C. Basdogan, "Robust repetitive controller for fast AFM imaging," *Nanotechnology, IEEE Transactions on*, vol. 10, no. 5, pp. 1074–1082, 2011.
- [24] G. Schitter, A. Stemmer, and F. Allgöwer, "Robust two-degree-of-freedom control of an atomic force microscope," *Asian Journal of Control*, vol. 6, no. 2, pp. 156–163, 2004.
- [25] P. Heuvel, M. A. Kulakov, and B. Bullemer, "An adaptive scan generator for a scanning tunneling microscope," *Review of Scientific Instruments*, vol. 65, no. 1, pp. 89–92, 1994.
- [26] A. Ahmad, A. Schuh, and I. W. Rangelow, "Adaptive AFM scan speed control for high aspect ratio fast structure tracking," *Review of Scientific Instruments*, vol. 85, no. 10, p. 103706, 2014.
- [27] J. Ren and Q. Zou, "Adaptive-scanning, near-minimum-deformation atomic force microscope imaging of soft sample in liquid: Live mammalian cell example," in *American Control Conference (ACC), 2016.* IEEE, 2016, pp. 1235–1240.
- [28] K. Wang, C. Manzie, and D. Nešić, "Extremum-seeking-based adaptive scan for atomic force microscopy," in *Decision and Control (CDC), 2017 IEEE 56th Annual Conference on.* IEEE, 2017, pp. 2114–2119.
- [29] M. Haring, N. Van De Wouw, and D. Nešić, "Extremum-seeking control for nonlinear systems with periodic steady-state outputs," *Automatica*, vol. 49, no. 6, pp. 1883–1891, 2013.
- [30] B. P. Lathi, *Linear systems and signals.* Oxford University Press, 2009.
- [31] D. Croft, G. Shed, and S. Devasia, "Creep, hysteresis, and vibration compensation for piezoactuators: atomic force microscopy application," *Journal of Dynamic Systems, Measurement, and Control*, vol. 123, no. 1, pp. 35–43, 2001.
- [32] Y. K. Yong, S. O. R. Moheimani, B. J. Kenton, and K. K. Leang, "Invited review article: High-speed flexure-guided nanopositioning: Mechanical design and control issues," *Review of Scientific Instruments*, vol. 83, no. 12, p. 121101, 2012.
- [33] G.-Y. Gu, L.-M. Zhu, C.-Y. Su, and H. Ding, "Motion control of piezoelectric positioning stages: modeling, controller design, and experimental evaluation," *IEEE/ASME Transactions on Mechatronics*, vol. 18, no. 5, pp. 1459–1471, 2013.
- [34] A. J. Fleming and S. R. Moheimani, "A grounded-load charge amplifier for reducing hysteresis in piezoelectric tube scanners," *Review of Scientific Instruments*, vol. 76, no. 7, p. 073707, 2005.
- [35] A. Esbrook, X. Tan, and H. K. Khalil, "An indirect adaptive servocompensator for signals of unknown frequencies with application to nanopositioning," *Automatica*, vol. 49, no. 7, pp. 2006–2016, 2013.
- [36] A. Pavlov, N. van de Wouw, and H. Nijmeijer, "Frequency response functions for nonlinear convergent systems," *IEEE Transactions on Automatic Control*, vol. 52, no. 6, pp. 1159–1165, 2007.
- [37] B. A. Francis and W. M. Wonham, "The internal model principle of control theory," *Automatica*, vol. 12, no. 5, pp. 457–465, 1976.
- [38] Y. R. Teo, Y. Yong, and A. J. Fleming, "A comparison of scanning methods and the vertical control implications for scanning probe microscopy," *Asian Journal of Control*, 2016.
- [39] T. McKelvey, "Subspace methods for frequency domain data," in *American Control Conference, 2004. Proceedings of the 2004.* IEEE, 2004, pp. 673–678.
- [40] H. K. Khalil, *Nonlinear systems (3rd ed.)*. Upper Saddle River, NJ: Prentice Hall, 2002.



Kaixiang Wang received his B.E. degree in mechanical engineering from Beijing Institute of Technology and B.E. (Hons) degree in mechatronic systems from the Australian National University in 2014. He is currently in the final stage of his Ph.D. study with the Department of Mechanical Engineering at the University of Melbourne. His thesis investigates the modelling and adaptive scan strategy of atomic force microscopy (AFM).

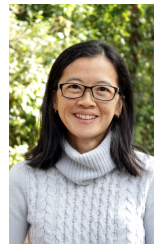


Dragan Nesic (F'08) is a Professor in the Department of Electrical and Electronic Engineering (DEEE) at The University of Melbourne, Australia. He received his BE degree in Mechanical Engineering from The University of Belgrade, Yugoslavia in 1990, and his Ph.D. degree from Systems Engineering, RSISE, Australian National University, Canberra, Australia in 1997. Since February 1999 he has been with The University of Melbourne. His research interests include networked control systems, reset systems, extremum seeking control, hybrid control systems, and so on. He was a co-recipient of the George S. Axelby Outstanding Paper Award (2018). He was also awarded a Humboldt Research Fellowship (2003) by the Alexander von Humboldt Foundation, an Australian Professorial Fellowship (2004-2009) and Future Fellowship (2010-2014) by the Australian Research Council. He is a Fellow of IEEE. He served as a Distinguished Lecturer of CSS, IEEE and as a Member of the Board of Governors, CSS, IEEE. He also served as an Associate Editor for the journals *Automatica*, *IEEE Transactions on Automatic Control*, *Systems and Control Letters*, *European Journal of Control* and as a General Co-Chair of IEEE CDC 2017 in Melbourne. Currently, he serves as an Associate Editor for the *IEEE Transactions on Control of Network Systems* (CONES).



Michael G. Ruppert (M'14) received the Dipl.-Ing. degree in automation technology in production from the University of Stuttgart, Germany, in 2013 and the Ph.D. degree in electrical engineering from The University of Newcastle, Australia in 2017. As a visiting researcher, he was with The University of Texas at Dallas, USA from 2015 until 2016 and he is now a lecturer at The University of Newcastle. His research interests include the utilization of system theoretic tools for sensing, estimation and control in high-speed and multifrequency atomic

force microscopy. Dr Ruppert held an Academic Merit Scholarship from the University of Stuttgart, the Baden-Württemberg Scholarship and post-graduate research scholarships with The University of Newcastle and CSIRO, Clayton, VIC, Australia. Dr Ruppert's research has been recognized with the 2013 IEEE/ASME AIM Best Conference Paper Finalist Award, the 2017 University of Newcastle Higher Degree by Research Excellence Award, the 2018 MARSS Best Conference Paper Finalist Award and the 2018 IEEE TCST Outstanding Paper Award.



Yuen Kuan Yong (M'09) is an associate professor at The University of Newcastle, Australia. Her research interests include nanopositioning systems, design and control of micro-cantilevers, atomic force microscopy, and miniature robotics. She was an Australian Research Council DECRA Fellow from 2013 to 2017. She is also the recipient of the University of Newcastle Vice-Chancellor's Award for Research Excellence in 2014, and the Vice-Chancellor's Award for Research Supervision Excellence in 2017. She is an associate editor for the

IEEE/ASME Transactions of Mechatronics.



Chris Manzie (SM'14) is a Professor and Head of Department of Electrical and Electronic Engineering at the University of Melbourne. His research interests are in model-based and model-free control and optimisation, with applications in a range of areas including systems related to energy, transportation and mechatronics and autonomous systems. He received an Future Fellowship from the Australian Research Council for the period 2012-2015. Professor Manzie was also a Visiting Scholar with the University of California, San Diego in 2007 and a Visiteur

Scientifique at IFP Energies Nouvelles, Rueil Malmaison in 2012. He is or has been an Associate Editor of *IEEE Control Systems Technology*, *IEEE Mechatronics*, *Elsevier Control Engineering Practice* and *ASME Mechatronics*.